Elizabeth G. Kelley, Paul D. Butler, Michihiro Nagao

4 Collective dynamics in model biological membranes measured by neutron spin echo spectroscopy

Thermal fluctuations and mechanical properties in lipid bilayers

Abstract: Cell membranes are extraordinarily heterogeneous environments composed of many thousands of chemically distinct lipids, sterols, and proteins. It is this very complexity and diversity in membrane composition that allows for its many varied and critical biological functions. These membranes are rather thin, only 3 to 5 nm thick, and present both structural and dynamic features on a wide variety of length and timescales. Within the hierarchy of length and timescales, the membrane's mechanical properties control many of the key functions such as bilayer shape transformations, protein binding, budding, and molecular transport which in turn are related to such things as apoptosis, endocytosis, protein signaling, and drug delivery. In this chapter, we will review how the elastic properties of membranes control the membranes' dynamics by presenting experimental results obtained by means of neutron spin echo spectroscopy. Toward the end of the chapter, we will consider another interesting property, membrane viscosity, and discuss some future aspects and challenges.

Keywords: lipid, membrane, dynamics, neutron scattering, neutron spin echo, bending modulus, area compressibility modulus, membrane viscosity

4.1 Introduction

The biological functions of lipid membranes require that they be highly dynamic. The hydrophobic tails rapidly flex and kink while the individual lipid molecules rotate, protrude, and diffuse on picosecond to nanosecond timescales [1, 2]. Biomembranes are also strikingly fluid with lipid diffusion coefficients on the order of 10^{-8} cm^2/s,

Elizabeth G. Kelley, NIST Center for Neutron Research, National Institute of Standards and Technology, Gaithersburg, USA
Paul D. Butler, NIST Center for Neutron Research, National Institute of Standards and Technology, Gaithersburg, USA; Department of Chemical & Biomolecular Engineering, University of Delaware, Newark, USA; Department of Chemistry, University of Tennessee, Knoxville, USA
Michihiro Nagao, NIST Center for Neutron Research, National Institute of Standards and Technology, Gaithersburg, USA; Center for Exploration of Energy and Matter, Department of Physics, Indiana University, Bloomington, USA

https://doi.org/10.1515/9783110544657-004

meaning a lipid molecule can diffuse across a typical cell length in less than 10 s [3, 4]. The fast local dynamics of the molecules allow the cell to easily manipulate the lateral membrane organization necessary for protein–protein interactions and cell signaling [5–7]. At the same time, the membrane must bend, bud, and fuse on much larger length scales as cells take in nutrients, send chemical signals, and even grow and divide [8, 9]. There is a large gap in length scale and timescale between the molecular and macroscopic processes that is bridged by the collective membrane dynamics shown in Figure 4.1. These mesoscale fluctuations involve tens to hundreds of lipids on the length scale of nm to μm and have their own role to play in the membrane's biological functions.

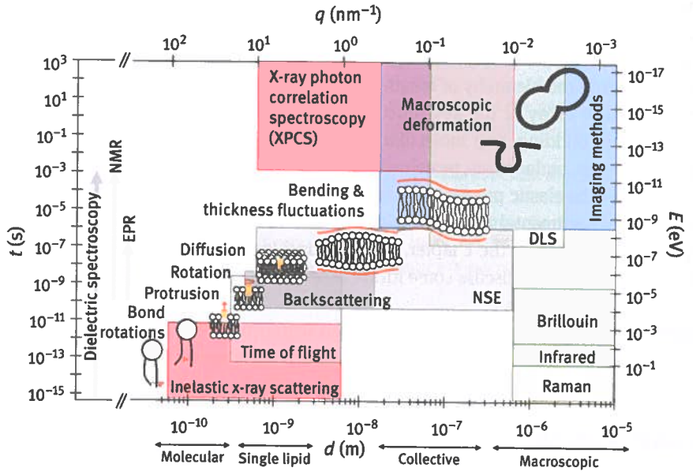

Figure 4.1: The length (*d*) and timescales (*t*), and corresponding momentum (*Q*) and energy (*E*) transfers, covering the hierarchy of membrane dynamics. The dynamic ranges of the spectroscopic techniques available to measure the different dynamics are also shown, with neutron techniques as gray squares, X-ray in red, light in green, and fluorescence and optical imaging techniques in blue. Spectroscopic techniques such as dielectric spectroscopy, nuclear magnetic resonance (NMR), and electron paramagnetic resonance (EPR) access a broad range of timescales without any specific associated length scales.

Stochastic membrane fluctuations, such as collective bending and thickness fluctuations, lead to small local changes in the membrane shape. These fluctuations were first observed in red blood cell plasma membranes as early as 1890 [10], and more than 125 years of research has revealed that the membrane shape changes are the result of both active and equilibrium processes [11]. At high frequencies, the

fluctuations are dominated by thermal excitations and are thought to play a role in preventing cell–cell adhesion and facilitate the diffusion of membrane-embedded proteins [12–17]. These same fluctuations affect membrane protein folding, channel formation, and function within the membrane [18–23], and play a significant role in cell adhesion [24–28], facilitating vesicle budding and trafficking [8, 29], and influencing cell spreading and motility [30–32]. Moreover, changes in membrane fluctuations have been directly linked to cell function and disease. Studies of macrophages show that the membranes are softer and have a greater fluctuation amplitude when the cells are activated, which likely aides in phagocytosis as the cells engulf foreign bodies [33, 34]. Changes in the fluctuation spectrum of red blood cell membranes also are seen after malaria and parasite infections [35, 36], as well as in sickle cell diseases [37–39], and studies suggest that cancer cells are softer than nonmalignant cells, which may contribute to the blebbing and migration of cancerous cells [40–42]. As such, measuring and quantifying the membrane fluctuations have important implications for understanding both biomembranes and cell functions.

This chapter focuses on measuring the equilibrium undulations in model lipid membranes, namely the mesoscale collective bending and thickness fluctuations, and how the measurements can be used to quantify the membrane elastic and viscous properties. Both of these dynamic processes are a direct consequence of the membrane being soft. As illustrated in Figure 4.1, the bending fluctuations are undulations normal to the membrane plane at a constant membrane thickness (often referred to as height fluctuations) [12, 43–45], while thickness fluctuations are undulations of the two membrane leaflets in opposite directions (sometimes referred to as peristaltic or breathing modes) [46–50]. The fluctuation length scales are dictated by the membrane elastic properties, or how resistant the membrane is to bending or compressing in solvent [51–53], the same properties that determine the energy required for the large-scale membrane deformations that occur in cell processes with macroscopic membrane remodeling. Meanwhile, the thickness fluctuation timescale will be determined by the membrane compressibility and how long it takes the lipids to flow as the membrane relaxes – or the membrane viscosity [53] – the same viscosity that dictates the timescales of molecular lipid and protein diffusion in the membrane that we talked about at the beginning of this chapter [54–57]. In other words, the collective fluctuations are governed by the same properties that influence the microscopic and macroscopic membrane functions, and measuring these dynamics gives us a way to quantify both the elastic and viscous properties that are essential to biological membrane functions.

While the mesoscale dynamics are an important bridge between the microscopic and macroscopic scales, accessing the length and timescales necessary to study the collective fluctuations can be experimentally challenging. Biological membranes are on the order of 5 nm thick, meaning we need to be able to resolve bending fluctuations on sub-nanometer scales. Similarly, theory and experiment suggest that thickness fluctuation amplitudes are on the order of 20% of the membrane thickness [47, 52,

58, 59] – or ≈ 1 nm – and estimates from the membrane viscosity tell us that these fluctuations should relax on nanosecond timescales [53]. These dynamics are too slow for traditional spectroscopic techniques such as NMR [2, 60–62], Raman [63–65], infrared [64, 66], dielectric [67], and EPR [68–70] that are sensitive to the motions of fatty acyl tails and the individual lipid molecules. On the other hand, the dynamics are too small and too fast for most light scattering and microscopy methods that are used to study large-scale dynamics and shape changes [34, 71–74]. As illustrated in Figure 4.1, neutron spectroscopy techniques cover a range of length scales and timescales that are hard to access with other characterization techniques and are therefore uniquely suited for characterizing the collective membrane fluctuations. This chapter will focus on neutron spin echo (NSE) spectroscopy and how this technique can be used to measure the collective bending and thickness fluctuations to determine the membrane elastic and viscous properties.

The remainder of this chapter is structured as follows: Section 4.2 presents the basics of neutron scattering and how NSE works. Section 4.3 covers the theoretical background necessary to correlate membrane dynamics with experimental NSE data. In Section 4.4, example NSE measurements of collective bending and thickness fluctuations are presented. A summary and current and future challenges close out the chapter in Section 4.5.

4.2 The NSE Technique

Neutrons are noncharged particles (neutron mass $m_n = 1.67 \times 10^{-27}$ kg) [75] that have both particle and wavelike properties. A free neutron has momentum $\vec{p}_n = \hbar\vec{q}$, where $\vec{q}$ is the wavevector of the associated wave function and $\hbar = h/2\pi$ with h as Planck's constant. $\vec{q}$ describes the propagation direction and speed of the wave with a magnitude $|\vec{q}| = q = m_n v_n/\hbar = 2\pi/\lambda$, where v_n is the velocity of the neutron and λ is its wavelength. Typical neutron wavelengths range from 0.1 to 2 nm, which allows neutron scattering techniques to provide detailed structural information on the nanometer scale. Several neutron scattering methods covered in other chapters illustrate the capability of neutron scattering to provide important information about the lipid bilayer thickness, composition, and asymmetry as well as protein binding and orientation in the membrane.

Neutron scattering also is an important tool for understanding nanoscale dynamics. The neutron energy is given by $E_n = \left|\frac{\vec{p}_n^2}{2m_n}\right|$ and is on the order of the thermal energy, $k_B T \approx 10$ meV (1 meV = 1.6×10^{-22} J = 2.42×10^{11} Hz). Neutron backscattering and time of flight instruments are capable of resolving 10^{-3} meV changes in neutron energy, providing dynamic information on picosecond to nanosecond timescales [76, 77]. These techniques mostly measure the incoherent or "self" dynamics – the correlations

between the relative positions of a given atom at different times – and are very useful for determining the diffusion of hydration water, lipids, and other small molecules embedded in lipid membranes [78–84].

Measuring collective membrane dynamics on the tens or hundreds of nanosecond timescales requires an instrument capable of measuring even smaller changes in neutron energy, also referred to as having a higher energy resolution. Measuring a relaxation time on the order of 100 ns requires resolving a change in neutron energy of ≈ 10 neV (10^{-8} eV!), which is currently only achievable using NSE, the highest energy resolution neutron spectroscopy technique [85]. NSE is capable of measuring these really small energy changes because it operates using fundamentally different principles from other spectrometers as we discuss in more detail in Section 4.2.3. Another important difference is that NSE is most suited to measuring the coherent dynamics – dynamics that originate from correlations between relative positions of different atoms at different times – or the exact collective dynamics we are interested in measuring in lipid membranes.

4.2.1 Basics of neutron scattering

A basic scheme of a scattering experiment is shown in Figure 4.2. Consider a neutron beam characterized by its wavevector $\vec{q}$. If the initial wave $\vec{q}_i$ interacts with a nucleus and scatters, then the final wave will have a different wavevector $\vec{q}_f$. Here, we can define the momentum transfer as

$$\hbar\vec{Q} = \hbar(\vec{q}_i - \vec{q}_f) \tag{4.1}$$

where $\vec{Q} = \vec{q}_i - \vec{q}_f$ is the scattering vector, often also referred to as the momentum transfer vector, while the corresponding energy transfer, ω, is defined as the difference between the initial, E_i, and final, E_f, waves

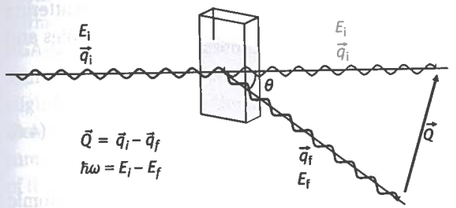

Figure 4.2: Schematic of the geometry of a scattering experiment. The initial neutron wave is characterized by its wavevector $\vec{q}_i$ and energy E_i. The initial wave interacts with the object and is scattered into scattering angle θ. The final neutron is characterized by its wavevector $\vec{q}_f$ and energy E_f. The scattering vector $\vec{Q}$ is expressed as $\vec{Q} = \vec{q}_i - \vec{q}_f$, and the energy exchanged is $\hbar\omega = E_i - E_f$.

$$\hbar\omega = E_i - E_f = \frac{\hbar^2}{2m_n}(q_i^2 - q_f^2) \tag{4.2}$$

Equations (4.1) and (4.2) express the momentum and energy conservation of the scattering process, respectively. Here, we consider the magnitude of $\vec{Q}$ by defining the angle between $\vec{q}_i$ and $\vec{q}_f$ as the scattering angle, θ, and applying $q_i \approx q_f$ ($\hbar\omega \approx 0$ *i.e.*, small energy transfer) as

$$\left|\vec{Q}\right| = Q = 2q_i \sin\left(\frac{\theta}{2}\right) = \frac{4\pi}{\lambda}\sin\left(\frac{\theta}{2}\right) \tag{4.3}$$

In the case of a perfectly ordered system, Bragg's law states that constructive interference will occur when $2d\sin\left(\frac{\theta}{2}\right) = n\lambda$, where d is the spacing between scattering planes and n is an integer. For such systems, Q is simply given as $Q = 2\pi/d$, demonstrating the inverse relationship between the length scales in the sample and the Q at which those length scales significantly impact the scattering. In other words, large length scales are associated with small Q values and vice versa. The primary aim of neutron scattering is to determine the probability of neutrons being scattered in $\vec{Q}$ with energy transfer ω, known as the dynamic structure factor $S(\vec{Q}, \omega)$. The Fourier transform of $S(\vec{Q}, \omega)$ with respect to ω is called the intermediate scattering function (ISF), $I(\vec{Q}, t)$, which can be written as

$$S(\vec{Q}, \omega) = \mathrm{FT}\left\{I(\vec{Q}, t)\right\} \tag{4.4}$$

$$I(\vec{Q}, t) = \left\langle \exp\left\{-i\vec{Q}\cdot\left[\vec{r}(t) - \vec{r}'(0)\right]\right\}\right\rangle \tag{4.5}$$

where $\langle\cdots\rangle$ indicates an ensemble average over all pairs of atoms, t is the time, and $\vec{r}$ and $\vec{r}'$ are position vectors for the atoms, respectively.

In a static elastic scattering experiment such as small-angle neutron scattering (SANS), we ignore the energy exchange between the neutrons and our samples and integrate the scattering over all neutron energies,

$$S(\vec{Q}) = \int S(\vec{Q}, \omega)d\omega \tag{4.6}$$

which corresponds to the Fourier transform of the instantaneous spatial atomic correlations in the system, that is, the structure of our sample. For the rest of the chapter, we only consider isotropic scattering cases for simplicity and treat the vector $\vec{Q}$ as a scalar Q. Measuring the membrane structure requires counting the number of neutrons scattered at angle θ or corresponding Q.

4.2.2 Inelastic/quasi-elastic scattering techniques

Measuring the dynamic structure factor, $S(Q, \omega)$, requires keeping track of the energy exchanged between the neutrons and the sample (ω) as these are scattered at a defined angle (θ or corresponding Q). This type of measurement is called inelastic or quasi-elastic neutron scattering. Information on the dynamic length scales is given by Q while information on the energy scales is given by ω. Most spectrometers determine the energy exchanged by analyzing the initial and final neutron energies. Therefore, in order to achieve higher energy resolution, narrow $\Delta\lambda/\lambda$ (or $\Delta v_n/v_n$) of the initial neutron beam is required. The need for a narrow wavelength distribution drastically limits the number of useful neutrons, and a scattering experiment with the high energy resolution needed to measure relaxation processes on the order of 100 ns would be impossible because of poor counting statistics. Ferenc Mezei, who invented the NSE principle in 1972 [85], illustrates the severity of this limitation in the first text book on NSE [86]. According to his estimates, achieving an energy resolution of 50 neV on an ideal hypothetical time of flight instrument would not count more than one neutron a day in the detector, which means it would take literally years to get any useful information on the sample dynamics. As explained below, his proposed NSE technique broke through this limitation and significantly improved the energy resolution by eliminating the requirement for a narrow $\Delta\lambda/\lambda$.

4.2.3 Characteristics of the NSE technique

Currently, the best NSE instrument in the world (IN15 in Grenoble, France) has an energy resolution of a few neV (or a few μs) while using a wavelength distribution $\Delta\lambda/\lambda$ on the order of 10% [87], ensuring sufficient neutron flux to perform the scattering experiments. There are a handful of NSE instruments in operation around the world [86–95], with more under construction [96]. There are two spectrometers in North America: the SNS-NSE at Oak Ridge National Laboratory [95] and the NGA-NSE (formerly NG5-NSE) at the National Institute of Standards and Technology [91]. The NGA-NSE is a reactor-based instrument while the SNS-NSE is at a spallation neutron source. The instrument design and operation for reactor versus spallation sources are slightly different due to the differences in the neutron source; however, both instruments operate on the same basic principles outlined below. We note that the quantum mechanical description and details of NSE instrumentation are beyond the scope of this Chapter, and we instead refer the interested reader to a textbook on NSE [92] as well as publications on specific spectrometers [97, 98] for more information.

NSE measures dynamics by taking advantage of the fact that neutrons have a spin. Although a neutron has no net charge, it has a spin degree of freedom of 1/2, which gives the neutron a magnetic moment. The NSE technique uses polarized neutrons, meaning only one state of the neutron spin is selected from the initial neutron beam.

That polarized beam then passes through a variety of magnetic fields as it traverses the instrument, through the sample and onto the detector. The trick to NSE's high energy resolution is to make use of the Larmor precession of the neutron spin in a magnetic field to provide each neutron with an "internal" clock with which to track any change in neutron velocity (or equivalently energy, $E_i = m_n v_i^2/2$) [85, 86, 92]. When the neutron spin direction is parallel to a magnetic field, the polarization of the spin state is maintained. On the other hand, when the neutron spin is perpendicular to the magnetic field, the spin starts to rotate around the magnetic field (called Larmor precession), shown schematically in Figure 4.3b. The neutron spins will precess with a frequency, $\omega_L = -\gamma_L B$ in which γ_L is the Larmor constant for a neutron and B is the average field strength, and the precession angle is proportional to the time the neutron spends in the magnetic field: $\varphi_L = \omega_L t = \omega_L l/v \propto B\lambda$ where l is the length of the field. Larmor precession is the same process that is key to NMR (for nuclear spin of various kinds of nuclei) and EPR (for electron spin) spectroscopic techniques that are also used to measure membrane dynamics [61, 70].

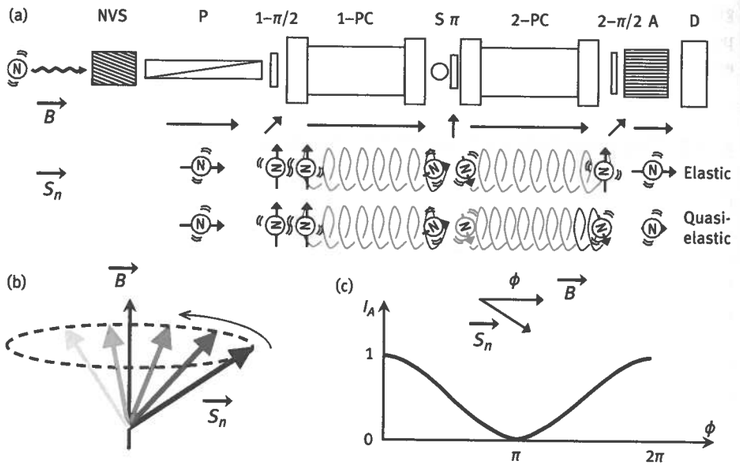

Figure 4.3: (a) A schematic illustration of a reactor-based NSE instrument, which consists of a neutron velocity selector (NVS), a neutron polarizer (P), the first and second $\pi/2$ flippers (1-$\pi/2$ and 2-$\pi/2$), precession fields (1-PC and 2-PC) before and after the sample (S), a π flipper, a neutron spin analyzer (A), and a neutron detector (D). Also the instrumental magnetic field direction $\vec{B}$ and neutron spin direction $\vec{S}_n$ for elastic and quasi-elastic scattering cases are shown. (b) A neutron spin $\vec{S}_n$ is subject to the Larmor precession in a magnetic field $\vec{B}$. (c) The spin analyzer allows neutrons to pass through with cosine probability of $\vec{S}_n$ along $\vec{B}$, namely $I_A = (1 + \cos\phi)/2$.

In NSE, information about the initial velocity is encoded within the neutron itself through Larmor precession, and the initial velocity can be compared with the final velocity for the same neutron. Figure 4.3a shows a layout of a NSE instrument. The basic idea is the following: The incident neutron wavelength and wavelength distribution are defined using a neutron velocity selector (NVS). The beam is then polarized by passing the neutrons through a polarizer (P) to select one state of neutron spins. The polarized neutrons are then flipped perpendicular to the magnetic field by a so called $\pi/2$-flipper (1-$\pi/2$). The precession frequency is controlled by a magnetic field in the main precession coil along the flight path from the $\pi/2$-flipper to the sample (1-PC). After the sample, a π-flipper reverses the precession angle and the neutrons pass through a second precession field (2-PC). A second $\pi/2$-flipper (2-$\pi/2$) stops the precession and the beam passes through a spin analyzer (A) and hits the detector (D). The spin analyzer only allows the cosine probability of the neutron spin direction parallel to the magnetic field to pass through to the detector. Figure 4.3c shows the neutron intensity I_A transmitted through the analyzer with the angle between the magnetic field and the neutron spin defined as ϕ, the net change in precession angle after passing through the two precession fields. In this case, I_A can be written as $I_A = (1 + \cos\phi)/2$. If the sample scatters elastically, that is, $\hbar\omega = 0$, then there is no net change in neutron spin after passing through both precession fields and the initial polarization is recovered, therefore $\phi = 0$ and $I_A = 1$ (Figure 4.3a). The precession angles in the primary (1-PC) and secondary (2-PC) paths are only different when the symmetry is distorted because of a change in the neutron velocity after interacting with the sample, that is, the neutrons scatter quasi-elastically, and both $\phi \neq 0$ and $\hbar\omega \neq 0$. In this case, the final spin polarization is rotated by an angle ϕ from the initial polarization leading to a decrease in the measured intensity, I_A, at the detector. Using this set-up unique to NSE, it is possible to make extremely accurate measurements of the energy change during the scattering process, and therefore to design a spectrometer with high resolution.

The reason NSE can use a relatively broad wavelength distribution and still provide a high energy resolution is because the energy resolution of the neutrons (determined by the distribution of velocity v_n or wavelength λ) is decoupled from the resolution of the energy transfer with the sample (determined by measuring the change in each neutron's polarization). This characteristic allows NSE to be the highest energy resolution technique among neutron spectroscopies with good counting statistics within a realistic experimental time. Furthermore, the measured neutron intensity can be written as $I \propto \int S(Q,\omega)\cos(\omega t)d\omega$ because the spin analyzer only allows the cosine probability of the neutron spin direction (I_A) to pass through to the detector. This equation is a cosine Fourier transformation of $S(Q,\omega)$, equivalent to $I(Q,t)$, meaning NSE automatically provides results in the time domain, while all the other neutron spectrometers work in the energy domain (see eqs. (4.4) and (4.5)). Because NSE works in the time domain, it is best suited to measuring relaxation processes (quasi-elastic scattering) rather than excitation processes (inelastic

scattering). In NSE, we define the Fourier time as $t \equiv 2\pi\gamma_L \left(\frac{m_n}{h}\right)^2 \lambda^3 J$, where J is the magnetic field (B) integral along the neutron trajectory, $J = \int B dl$.

Figure 4.4 shows a schematic image of $I(Q,t)$ measured in a scattering experiment. Figure 4.4a shows the correlation function (scattering intensity $I(Q,t)$) with respect to space (Q) and time (t). NSE measures the normalized ISF $I(Q,t)/I(Q,0)$, which is used to describe the Q-dependent time correlation function as shown in Figure 4.4b.

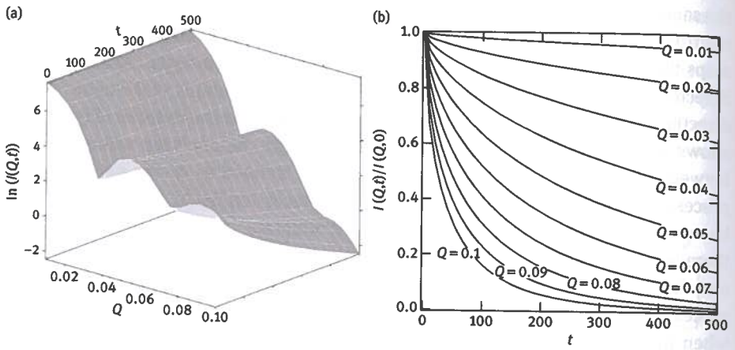

Figure 4.4: A typical example of $I(Q,t)$ in (a) three-dimensional representation as Q and t dependence of $\ln[I(Q,t)]$ and (b) representation of the normalized intermediate scattering function $I(Q,t)/I(Q,0)$ against t. $I(Q,t=0)$ in (a) corresponds to the Fourier transform of the instantaneous spatial atomic correlations, that is, structure, and the time decaying $I(Q,t)$ corresponds to how fast the structural correlation is lost with t due to the motions at the corresponding length scale Q.

4.3 Membrane dynamics theory

Membranes in solutions have very large interfacial area. When 0.01 mol of surfactant are dispersed in a liter of water (corresponding to a mole fraction of 10 mmol/L), the total interfacial area of the self-assembled bilayers is on the order of 10^3 m^2, or roughly the size of a football pitch, in just 1 L of water. (A typical head area per molecule is ≈ 0.7 nm^2 while the bilayer thickness is on the order of nm). Therefore, interfacial energy plays a decisive role in determining the shape of the membranes.

The framework for understanding the curvature elasticity of lipid bilayers was established in a seminal paper by Helfrich in 1973 [12]. Because the bilayer is thin and governed by the interfacial energy, he assumed that the bilayer was infinitely thin and wrote the bending energy as what has become known as the Helfrich Hamiltonian

$$F = \int dA \left[\frac{\kappa}{2}(C_1 + C_2 - C_s)^2 + \bar{\kappa} C_1 C_2\right] \tag{4.7}$$

where C_1 and C_2 are the two principal curvatures of a membrane, C_s is the spontaneous curvature, κ is the bilayer bending modulus, and $\bar{\kappa}$ is the saddle-splay modulus, respectively, and the integration is over the area A. The Gauss–Bonnet theorem can be applied to the second term of eq. (4.7) as $\int C_1 C_2 dA = 4\pi$. The saddle-splay modulus $\bar{\kappa}$ is sensitive to topological changes of the membrane. However, in NSE experiments, the membrane topology does not change and this term is almost constant. Also, if the lipid membrane is fluid and there are no long-range interactions present, a special surface within the bilayer can be defined such that $\bar{\kappa} = 0$ [43, 45], which further supports that the second term in the Helfrich Hamiltonian can be neglected in certain cases.

The interfacial energy also contains a contribution from the elastic energy required to stretch the membrane (which originate from the membrane tension) and is written as a function of the relative area change $\Delta A/A$. However, an area change requires a large compression energy, particularly for short wavelengths, which implies that the surface tension is zero for free unstressed membranes [44, 99]. Further, in order to assume that the interfacial tension is finite, the area change in the membrane must be compensated for by either adding or removing lipids from the bilayer, meaning there would need to be a reservoir of lipid molecules [100]. Technically, there is a very low concentration of free lipids present in the solution and the bilayer can exchange lipid molecules with the solvent; however, the timescales for lipid exchange are orders of magnitude slower than the timescales of the membrane fluctuations and the lipid exchange cannot compensate for the area changes due to the membrane bending [12]. Early work by Faucon et al. included a stretching contribution when analyzing the thermal undulations of giant unilamellar vesicles (GUV, typical sizes on the order of μm) that were measured using an imaging technique [71]. From their analysis, the estimated surface tension was on the order 10^{-5} N/m. However, later work by Yeung and Evans suggested that the dynamics measured by Faucon et al. could also be explained by taking an internal membrane friction into account [101], which will be explained later in Section 4.3.2.

The description of the membrane interfacial energy according to the Helfrich Hamiltonian is an essential starting point to understanding membrane bending dynamics, but the model neglects any change in membrane thickness or internal membrane structure. As we have learned more about the structure and dynamics of lipid bilayers, the models for the membrane deformation energy have also evolved to take into consideration many other contributions. As suggested above, Yeung and Evans and several others have proposed that lipid membrane undulations are affected by an internal membrane friction – a result of the membrane being composed of two monolayers as will be discussed more in Section 4.3.2 [53, 101–103]. In some membranes, the lipid molecules also are tilted with respect to the membrane normal [104, 105]. This

molecular tilt is neglected in Helfrich's original free energy expression [12], but more recent studies have shown that the membrane internal structure does contribute to the membrane energy through a molecular tilt modulus [106–112].

In the following subsections, we describe the theory for the membrane dynamics as it applies to NSE measurements. The models for NSE data build in complexity with each subsequent subsection as the theory evolves and more details of the membrane structure are considered.

4.3.1 Single membrane fluctuation dynamics and intermediate scattering function

Because this chapter is about studying lipid bilayer dynamics with NSE, we start with a model for the $I(Q,t)$ (which we directly measure with NSE, see Section 4.2.3) based on the Helfrich bending Hamiltonian that was derived by Zilman and Granek (ZG) [99, 113]. At short time, t, and length, l, scales ($t \lesssim 1$ μs and $l \lesssim L$ with L a long length scale cutoff), most membranes can be treated as an assembly of independent and nearly flat membrane sheets. The length scale L depends on the experimental system studied and is defined as the plaquette linear size, which is considered as the pore size in a sponge phase, the Helfrich–Servuss patch size (corresponding to the intermembrane collision length) in a lamellar phase, or the vesicle radius.

4.3.1.1 Single membrane fluctuation dynamics – Zilman and Granek approach

When a nearly flat thin elastic sheet is thermally undulating at a height, $h(\vec{r})$, from a mean surface as illustrated in Figure 4.5, the Helfrich bending Hamiltonian is proportional to the square of the curvature and takes the following form [99, 113]

$$F = \frac{\kappa}{2}\int d^2r\left[\nabla^2 h(\vec{r})\right]^2 = \frac{\kappa}{2L^2}\sum_{\vec{k}} k^4 h_{\vec{k}} h_{-\vec{k}} \tag{4.8}$$

Here, $\vec{r}$ is a two-dimensional vector (x,y) on the planar surface and $h(\vec{r})$ is the local height of the surface (by definition $\langle h(\vec{r})\rangle = 0$). As discussed earlier, the spontaneous curvature of the bilayer is assumed to be zero. The second equality expresses the Hamiltonian in terms of Fourier modes, where $h_{\vec{k}} = \int d^2r h(r) e^{i\vec{k}\cdot\vec{r}}$ is the two-dimensional Fourier transform of $h(\vec{r})$. We note here that different communities have different notations. In this chapter, we are using $\vec{k}$ rather than $\vec{q}$ to denote the Fourier component of the membrane fluctuations and use $\vec{q}$ and $\vec{Q}$ to denote the wavevector and the scattering (or momentum transfer) vector, respectively, as defined in the previous section on scattering. L is the membrane patch size, where we consider the dynamics of a membrane plaquette. The membrane is suspended in

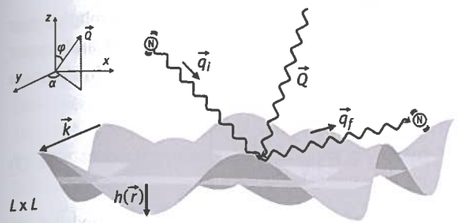

Figure 4.5: A schematic representation of undulating thin sheet around a flat reference surface (shown in light gray) in a plaquette size $L \times L$. The coordination axes are shown in the left corner. The undulations occur with height $h(\vec{r})$ about a nearly flat reference surface in the x, y plane where $\vec{r} = (x, y)$. Also defined are the membrane fluctuation wavevector $\vec{k}$ and the initial and final neutron wavevectors $\vec{q}_i$ and $\vec{q}_f$. The scattering vector is defined as $\vec{Q} = \vec{q}_i - \vec{q}_f$. The vector $\vec{Q}$ in the coordination axes is represented to define the angles for the orientational average (see eq. (4.19)).

aqueous solvent with solvent viscosity, η, and performs thermal undulations that are coupled to the hydrodynamic flow of the solvent. Applying the equipartition theorem to eq. (4.8) leads to the following expression for the equilibrium spectrum of undulations [114]

$$\langle h_{\vec{k}} h_{-\vec{k}}\rangle = \frac{k_B T L^2}{\kappa k^4} \tag{4.9}$$

The time-dependent correlation function of $h_{\vec{k}}(t)$ thus follows an exponential decay from its equilibrium value [114]

$$\langle h_{\vec{k}}(t) h_{-\vec{k}}(0)\rangle = \frac{k_B T L^2}{\kappa k^4} e^{-\omega(k)t} \tag{4.10}$$

The relaxation frequency $\omega(k)$ can be determined from a standard hydrodynamic mode analysis [113–116]

$$\omega(k) = \frac{\kappa k^3}{4\eta}. \tag{4.11}$$

In order to calculate $I(Q,t)$, it is important to first calculate the two-point correlation function $\langle\left(h(\vec{r},t) - h(\vec{r}',0)\right)^2\rangle$. The two-point correlation function can be determined using either a Langevin equation for the undulating bilayers in viscous solvent [99, 113] or the stochastic field approach [114]. Both approaches give the correlation function as

$$\langle\left(h(\vec{r},t) - h(r',0)\right)^2\rangle = \frac{k_B T}{2\pi^2\kappa}\int_{\pi/L}^{\pi/d_0} \frac{d^2k}{k^4}\left(1 - e^{-\omega(k)t}\right) \tag{4.12}$$

where d_0 represents the size of a lipid molecule (molecular length). At $t \lesssim \eta d_0^3/\kappa$ (very short timescales), the calculation yields the simple diffusion of the monomers.

For $t \gtrsim \eta L^3/\kappa$ (long times), the integral saturates to a constant and the correlation has decayed. In the intermediate time range $\eta d_0^3/\kappa \ll t \ll \eta L^3/\kappa$, the lower and upper limits of the integration are replaced by zero and infinity, and the integration evaluates to [99, 113, 114]

$$\langle (h(\vec{r},t) - h(\vec{r}',0))^2 \rangle \simeq 0.17 \left[\sqrt{\frac{k_B T}{\kappa}} \frac{k_B T}{\eta} t \right]^{2/3} \tag{4.13}$$

The above equation indicates that the membrane plaquette dynamics exhibit an anomalous $t^{2/3}$ time dependence and that the mean square displacement $\langle h(\vec{r})^2 \rangle$ follows $\kappa^{-1/3}$.

4.3.1.2 Intermediate scattering function

Now that we have a theoretical expression for the equilibrium height fluctuations – or correlations between the membrane heights as a function of time – that we can measure with NSE, we need to incorporate eq. (4.13) into $I(Q,t)$ to be able to fit experimental data. Considering a system containing a membrane plaquette, p, with a bilayer size of $L \times L$, the $I(Q,t)$ of the system is given by [99]

$$I(\vec{Q},t) = \frac{N_p}{V} \sum_p \left\langle e^{i\vec{Q}\cdot(\vec{R}_p(t) - \vec{R}_p(0))} \right\rangle I_p(\vec{Q},t) \tag{4.14}$$

where $\vec{R}_p$ is the center of mass position of the plaquette p, N_p is the number of molecules in a single plaquette, and V is the macroscopic system volume. The single plaquette ISF is [99, 113]

$$I_p(\vec{Q},t) = \frac{1}{N_p} \left\langle \sum_{i,j} e^{i\vec{Q}\cdot(\vec{R}_i(t) - \vec{R}_j(0))} \right\rangle \tag{4.15}$$

where $\vec{R}_i$ is the position vector of the ith lipid molecule in the center of mass coordinate frame and the sum runs over all molecules in a single plaquette.

The plaquette can also undergo simple diffusion, and in that case, the normalized ISF decays by contributions from both the diffusion and the membrane undulations as [117]

$$\frac{I(Q,t)}{I(Q,0)} = e^{-DQ^2 t} \frac{\langle I_p(\vec{Q},t) \rangle_{\vec{Q}}}{\langle I_p(\vec{Q},0) \rangle_Q} \tag{4.16}$$

where D is the center of mass diffusion constant of the patch, and the bracket indicates the average over all scattering angles (orientational average). For vesicles with ≈ 50 nm radius, the diffusion constant from the Stokes–Einstein equation is on the order of $10^{-12}\,\mathrm{m}^2/\mathrm{s}$. Therefore, for $t \ll \eta L^3/\kappa$, translational diffusion has a

negligible effect ($e^{-DQ^2 t} \approx 1$) and $I(\vec{Q},t)$ will be determined solely by individual membrane undulations. For the rest of this section, we will focus our attention on the plaquette undulations, neglecting contributions from translational diffusion. However, it is important to note that this simplification is not always possible. Depending on the vesicle size and concentration in the sample as well as Q and the Fourier times accessed in a particular experiment, the translational diffusion contribution to $I(\vec{Q},t)$ may need to be taken into account.

The internal position vector $\vec{R}_i(t)$ is now expressed in terms of the longitudinal two-dimensional vector $\vec{r}$ and the transverse component $h(\vec{r},t)$, and therefore, we can rewrite eq. (4.15) using a double integral as follows [99, 113]

$$I_p(\vec{Q},t) = \frac{1}{N_p d_0^4} \int d^2 r \int d^2 r' \left\langle e^{i\vec{Q}_\parallel \cdot (\vec{r} - \vec{r}')} e^{iQ_\perp [h(\vec{r},t) - h(\vec{r}',0)]} \right\rangle \tag{4.17}$$

where the scattering vector $\vec{Q}$ is decomposed into two component vectors: a longitudinal in-plane component, $\vec{Q}_\parallel$, and a perpendicular component $Q_\perp$. The membrane undulations are implicitly assumed to be small. Since $h(\vec{r},t)$ and $\vec{r}$ are weakly correlated, we assume that their averages can be decoupled. In the present treatment, the white noise appearing in the linear Langevin equation follows Gaussian statistics [99, 113, 114], which supports that we can assume that the statistics of $h(\vec{r},t)$ are also Gaussian [118]. This assumption relates the height fluctuations with the two-point correlation function, eq. (4.13), as follows [99, 117]

$$\left\langle e^{iQ_\perp [h(\vec{r},t) - h(\vec{r}',0)]} \right\rangle = e^{-\frac{Q_\perp^2}{2} \left\langle (h(\vec{r},t) - h(\vec{r}',0))^2 \right\rangle} \tag{4.18}$$

Note this equation is for a defined orientation while most lipid membrane samples are randomly orientated in solution. In order to apply the equation to isotropic structures, such as sponge, nonoriented lamellar, and vesicle structures, one needs to take the orientational average over all values of the angle between $\vec{Q}$ and the membrane normal, as [117]

$$I(Q,t) \equiv \langle I_p(\vec{Q},t) \rangle_{\vec{Q}} = \frac{1}{4\pi} \int_0^{2\pi} d\varphi \int_0^{\pi} \sin\alpha d\alpha I_p(\vec{Q},t) \tag{4.19}$$

The angles α and φ are defined in Figure 4.5. This average is assumed to be dominated by the region at $\varphi \approx 0$ ($Q_\parallel \approx 0$ and $Q_\perp \approx Q$) [113, 117]. At the limit of $\kappa \gg k_B T$, the solution to the integral is approximated as a pure stretched exponential decay [99, 113, 117, 119]

$$\frac{I(Q,t)}{I(Q,0)} \simeq e^{-(\Gamma_{ZG} t)^{2/3}} \tag{4.20}$$

where the decay rate Γ_{ZG} is

$$\Gamma_{ZG} = 0.025\sqrt{\frac{k_BT}{\kappa_{ZG}}}\frac{k_BT}{\eta}Q^3 \tag{4.21}$$

We now have a series of equations that relates the membrane bending modulus to the collective height fluctuations that are experimentally measured with $I(Q,t)/I(Q,0)$ – meaning we can quantify a membrane elastic property from our NSE measurement. In the original work, eq. (4.21) contained the intrinsic bending modulus, κ. Here, we replace κ with κ_{ZG} because, as we will see in Section 4.3.2, eq. (4.21) will only describe the intrinsic bending modulus in certain cases. Nevertheless, eq. (4.21) establishes that the measured decay rate is inversely related to the bending modulus and the expression gives the trends that you may intuitively expect – a stiff membrane with a large κ will have a lower decay rate and the measured correlations in $I(Q,t)$ will decay slower than a softer membrane with a lower κ.

It is noted here that both the transverse and longitudinal contributions to the scattering have been calculated by Zilman and Granek [99]. These calculations support that the longitudinal contribution is weak and the above description for only the transverse component is a good approximation for isotropically distributed bilayers as long as $\kappa \gg k_BT$. For works that consider the longitudinal, in-plane contribution to the dynamics in aligned lipid bilayers, we refer the reader to works by Rheinstädter and colleagues [81, 120].

4.3.2 Internal membrane dissipation – two coupled monolayers

We just saw how the Helfrich model of the membrane as a thin, structureless sheet can be applied to NSE data analysis. However, we know that the lipid membrane is not structureless, but is in fact composed of two lipid monolayers. If there were no interactions between the monolayers, then they would be free to slide past each other. However, for the bilayer to be stable, the monolayers *need* to interact with each other through van der Waals interactions between the lipid tails. Yeung and Evans suggest that this interaction could lead to "hidden" degrees of freedom in the bilayer bending dynamics due to an internal viscous contribution [101].

A similar idea was also proposed by Seifert and Langer (SL), where by incorporating the effects of potential density variations in each leaflet due to the bending deformations, they suggested that a viscous mode contributed to the membrane fluctuations [102, 103]. For long wavelengths, as represented schematically in Figure 4.6a, bending fluctuations do not significantly perturb the lipid monolayer densities and the standard hydrodynamic theory holds. On the other hand, short fluctuation wavelengths, as depicted in Figure 4.6b, create defects due to the fact that the molecular redistribution required by the perturbation cannot happen quickly enough. As a result, the short wavelength fluctuations are governed by an effective

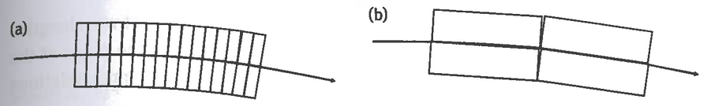

Figure 4.6: Schematic representation of a slightly bent membrane formed by multiple rectangles for (a) long wavelength undulation and (b) short wavelength undulation relative to the size of the lipid molecules. The bending imposes a radius of curvature that spreads the outer part of the rectangles out while compressing the inner portion. This requires the rectangular elements to distort to try to fill the voids and release the compression. For short time short wavelength modes the rectangles cannot accommodate the shape change fast enough, leading to an increase in the bending modulus of the membrane [102].

bending rigidity that is higher than the intrinsic bending modulus that controls the long wavelength fluctuations (*i.e.*, the short wavelength fluctuations require more energy than the long wavelength fluctuations). In order to mathematically express these physical effects, Seifert and Langer included a contribution from density modes in each monolayer to the free energy as [102, 103]

$$F = \int dA\left[\frac{\kappa}{2}(2H)^2 + \frac{K_A}{2}\left\{(\rho_m^+ + 2d_nH)^2 + (\rho_m^- - 2d_nH)^2\right\}\right] \tag{4.22}$$

where the mean curvature H has the relation $2H = C_1 + C_2$, K_A denotes the monolayer area compressibility modulus, $\rho_m^{\pm}$ is the scaled deviation of the projected density from its equilibrium value for a flat membrane, and d_n is defined as the distance between the mid-plane of the bilayer and the neutral surface of a monolayer. The neutral surface in eq. (4.22) is a special dividing surface where the monolayer neither stretches nor compresses as it is bent [45]. This mathematical definition greatly simplifies the expressions for the bilayer free energy; however, it cannot be measured experimentally making it difficult to assign a numerical value for d_n as we will revisit later in Section 4.4.

The relaxation frequencies for this free energy model are given as follows [102, 103]

$$\omega_1(k) \approx \begin{cases} \frac{\kappa}{4\eta}k^3, & k \ll k_1 \\ \frac{K_A}{2b}\frac{\kappa}{\tilde{\kappa}}k^2, & k_1 \ll k \ll k_2 \\ \frac{K_A}{\eta_m}\frac{\kappa}{\tilde{\kappa}}, & k_2 \ll k \end{cases} \tag{4.23}$$

$$\omega_2(k) \approx \begin{cases} \frac{K_A}{2b}k^2, & k \ll k_1 \\ \frac{\tilde{\kappa}}{4\eta}k^3, & k_1 \ll k \end{cases} \tag{4.24}$$

where $\tilde{\kappa} = \kappa + 2d_n^2K_A$ is a renormalized bending rigidity including the effect of the elastic stretching and compression, b denotes a friction coefficient for a phenomenological internal dissipation, and η_m is the monolayer surface viscosity. $\tilde{\kappa}$ now

accounts for the extra energy required to bend the membrane at short wavelengths. The crossover wavevectors $k_1 \equiv 2\eta K_A/b\tilde{\kappa}$ and $k_2 \equiv \sqrt{2b/\eta_m}$ separate the range of the characteristic dynamics into three regimes, shown in the plot of dispersion relations in Figure 4.7.

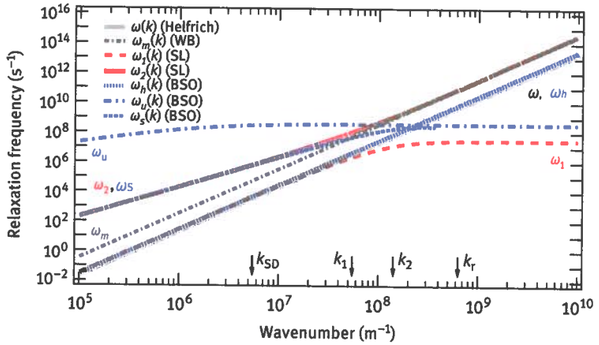

Figure 4.7: Comparison of the dispersion relations from the theories explained in this Section 4.3. The result for Helfrich is the solution of a standard hydrodynamic mode analysis (eq. (4.11)) shown as $\omega(k)$, and the modification of Watson and Brown (WB) gives $\omega_m(k)$. The theory by Seifert and Langer (SL) has two eigenvalues, ω_1 and ω_2 (eqs. (4.23) and (4.24)). The model by Bingham, Smye, and Olmsted (BSO) gives three independent eigenvalues, ω_h, ω_u and ω_s which are expressed in eqs. (4.34) to (4.36). $\omega_s(k)$ is not shown at high k values where the Stokes approximation breaks down, $k \gtrsim k_r$ ($k_r \equiv 2\pi/l_r$) [53]. The arrows at the bottom of the graph show the relevant length scales for the different theories. The parameters used in the calculation are given in the main text (see Section 4.3.4).

For long wavelength undulations (small k), $\omega_1(k)$ corresponds to the usual hydrodynamically damped bending mode and thus overlaps with the $\omega(k)$ predicted by the Helfrich theory. $\omega_2(k)$ is the damping rate of the slipping mode (density difference fluctuations between the monolayers that is damped by the inter-monolayer friction). For $k_1 \ll k$ (short wavelength undulations), $\omega_2(k)$ becomes the damping rate of the bending mode which is affected by the density mode because the lipid densities cannot respond quickly enough to changes in the membrane shape. Thus, an effectively larger bending rigidity $\tilde{\kappa}$ dominates the fluctuations. In this regime, the rate $\omega_1(k)$ is determined by the slipping mode. At the second crossover k_2, the main dissipative mechanism changes from inter-monolayer friction ($k \ll k_2$; slipping) to monolayer surface viscosity ($k_2 \ll k$; membrane hydrodynamics).

The dynamic undulation correlation function can be expressed as the sum of two decaying components as [101, 121–123]

$$\langle h_{\vec{k}}(t) h_{-\vec{k}}(0)\rangle = \frac{k_B T}{\kappa k^4}\left(A_1(k)e^{-\omega_1(k)t} + A_2(k)e^{-\omega_2(k)t}\right) \tag{4.25}$$

where $A_1(k) + A_2(k) = 1$ and

$$A_1(k) = \frac{\omega_2(k) - \kappa k^3/4\eta}{\omega_2(k) - \omega_1(k)} \tag{4.26}$$

A molecular dynamics simulation of a coarse-grained bilayer model has shown good agreement with this theory [123], and NSE data have provided evidence of the slipping mode in lipid bilayers [124, 125].

The ZG theory covered in Section 4.3.1.2 [99, 113] does not include these internal dissipation mechanisms, and as suggested earlier, eq. (4.21) will work for measurements of long wavelength fluctuations measured with dynamic light scattering (DLS, at small scattering vector Q) that are not affected by the internal membrane friction [126]. NSE measures the short wavelength fluctuations (large Q), where theory predicts that the inter-monolayer friction affects the dynamics. Early NSE measurements of lipid membrane bending fluctuations reported a much higher bending modulus than measured with other techniques [127–130]. These works used an effectively larger solvent viscosity (three to four times the actual solvent viscosity) as an additional dissipation mechanism to get κ values that were comparable to other experimental techniques [127–130]; however, from the theories described above, we now know that the additional dissipation mechanism comes not from the solvent, but from the inter-monolayer friction within the bilayer itself.

There are two ways to include the contribution from the density mode into NSE data analyses; one proposed by Watson and Brown (WB) [117, 119] and the other by the group of Monroy [124, 125]. We note here that, as alluded to in the previous section, the ZG theory has another limitation in that it does not properly account for the orientational averaging in the case when $\kappa \gg k_B T$ does not hold. However, this point is beyond the scope of this chapter and we encourage interested readers to refer to [131–134].

In the WB theory, they proposed a modification of the ZG theory to include contributions from the internal membrane friction into the NSE data analysis [117, 119]. Since the NSE timescale is relatively short, the energy dissipation from the surface viscosity is too slow to observe ($\omega_1(k)$ from the SL theory). Therefore, one can assume that the decay in the NSE time window is solely due to the bending modes and dominated by $\omega_2(k)$ [117], and eq. (4.25) becomes

$$\langle h_{\vec{k}}(t) h_{\vec{k}}(0)\rangle \approx \frac{k_B T}{\tilde{\kappa} k^4}\left(\frac{\tilde{\kappa} - \kappa}{\kappa} + e^{-\frac{\tilde{\kappa} k^3}{4\eta} t}\right) \tag{4.27}$$

We see that this correlation function is almost the same as the one presented in Section 4.3.1 for the ZG theory (eqs. (4.10) and (4.12)) except that we need to replace κ

with $\tilde{\kappa}$. Therefore, all the derivations described in Section 4.3.1 still hold, and the decay follows the stretched exponential function derived by Zilman and Granek. The only modification is to the expression for the relaxation rate, which now includes the effective bending modulus and becomes

$$\Gamma_{ZG_{mod}} = 0.025\sqrt{\frac{k_B T}{\tilde{\kappa}}}\frac{k_B T}{\eta}Q^3 \tag{4.28}$$

again with $\tilde{\kappa} = \kappa + 2d_n^2 K_A$ [117, 119]. This modification by Watson and Brown [117, 119], to include the internal membrane friction due to the inter-monolayer coupling, thus describes short wavelength membrane dynamics more accurately. This model was first applied to NSE data by Choi and colleagues [135], and gave a realistic number for κ, which supports the validity of the theory to explain short wavelength bending fluctuations without needing to use an effective solvent viscosity.

On the other hand, Arriaga et al. observed a deviation from the predicted Q^3 behavior of the relaxation rates measured by NSE (see e.g., eq. (4.28)). Instead, their data suggested a diffusive type Q^2 behavior for palmitoyl-oleoyl-phosphocholine (POPC) large unilamellar vesicles [124]. They ascribed the origin of this deviation to hybrid curvature-compression modes, equivalent to the models of inter-monolayer friction discussed in this section. They observed a crossover of Γ from Q^3 to Q^2 at $Q \approx 0.4\ \mathrm{nm}^{-1}$, where at low Q the usual bending type Q^3 relation is seen, while at high Q the dynamics scale with Q^2. Their observation yielded $K_A \approx 80$ mN/m, $b \approx 2\times10^9$ Pa·s/m, and $\kappa \approx 15\,k_BT$. Interestingly, the inter-monolayer friction constant b increased upon addition of cholesterol [124]. Mell and colleagues developed an expression for the ISF that includes the hybrid mode as [125]

$$\frac{I_{hyb}(Q,t)}{I(Q,0)} = e^{-0.3\frac{Rk_BT}{2d_0K_A}Q^2t^0} \tag{4.29}$$

where R is the radius of the vesicles. They showed that both the bending and hybrid modes contribute to the measured NSE data, while theory predicts that the hybrid mode dominates at high Q. As $I_{hyb}(Q,t)$ goes as $\exp(t^0)$, the hybrid mode is a non-decaying contribution seen at longer times. These examples suggest that NSE is sensitive to the internal membrane dynamical contributions and a careful evaluation of the theoretical underpinnings is essential to correctly interpret the data.

4.3.3 Dynamics of "thick" membranes

The original theory by Helfrich ignored any energetic contribution from the membrane structure [12]. While Yeung and Evans [101, 136] and Seifert and Langer [102, 103] successfully included inter-monolayer coupling as an additional dissipation mechanism in membranes, the models still neglect potential changes in the bilayer

thickness, even though thickness fluctuations in lipid bilayers have been theoretically predicted since the 1980s [19, 20, 46–48]. Computer simulations also have captured membrane thickness fluctuations [52, 108, 137–141]. Experimentally, the first direct observation of thickness fluctuations in surfactant membranes was made by Farago and colleagues in a stacked lamellar membrane [142, 143], and later more detailed experiments and analyses were performed by Nagao et al. [141, 144, 145] Thickness fluctuations in single component lipid bilayers were measured by Woodka and colleagues using NSE [58], and the method was then extended to a homogeneously mixed lipid membranes [59]. The experimental thickness fluctuation observations were also reproduced in recent computer simulations [141, 146]. Despite the growing experimental and computational data on the thickness fluctuations, a theoretical model that explicitly accounts for the dynamic contributions from the membrane thickness in the dispersion relation has only recently been developed by Bingham, Smye and Olmsted (BSO) [53].

The membrane geometry considered in the BSO model is schematically represented in Figure 4.8. The upper (+) and lower (−) monolayer surfaces are described by the height functions $h_+(\vec{r})$ and $h_-(\vec{r})$ from a planar reference plane (dashed straight line in Figure 4.8) as

$$h_+(\vec{r}) = d_+(\vec{r}) + s(\vec{r}) \tag{4.30}$$

$$h_-(\vec{r}) = -d_-(\vec{r}) + s(\vec{r}) \tag{4.31}$$

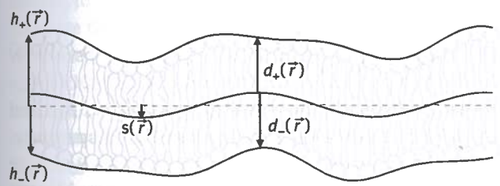

Figure 4.8: The membrane geometry considered in the Bingham, Smye and Olmsted model [53]. The monolayer height $h_\pm(\vec{r})$ is the surface height from the reference surface (shown as a dashed line). The monolayer thickness $d_\pm(\vec{r})$ is defined as the distance between the outer surface and the undulating mid-surface, $s(\vec{r})$.

where $d_\pm(\vec{r})$ is the monolayer thickness for each leaflet, and $s(\vec{r})$ is the height of the inter-monolayer surface from the reference plane. The free energy of each monolayer has been calculated in the framework of the Helfrich Hamiltonian [53]

$$F_\pm = \frac{1}{2}\int dA\left[\kappa_{m\pm}(\nabla^2 h_\pm)^2 + \gamma_{s\pm}(\nabla h_\pm)^2 + K_{A\pm}\left(\frac{d_\pm - d_{0\pm}}{d_{0\pm}} - d_{0\pm}\nabla^2 s\right)^2\right] \tag{4.32}$$

where $\kappa_{m\pm}$ is the monolayer bending modulus for each leaflet, $\gamma_{s\pm}$ is the surface tension which restricts variations in the monolayer/water interfacial area, and $d_{0\pm}$ is the unperturbed monolayer thickness, respectively. The total free energy was set as

$$F = F_+ + F_- + F_{frame} \tag{4.33}$$

where $F_{frame} = \frac{\gamma_{fr}}{2}\{\nabla(h_+ + h_-)\}^2$ is the contribution from a tension that restricts changes in the total membrane area with the frame tension, γ_{fr}. In this framework, Bingham *et al.* found three types of relaxation frequencies in a "thick" membrane [53].

The first mode is equivalent to the ripple type dynamic (bending) mode of Brochard and Lennon [116]. This mode appears in the model as a coupled bilayer and internal surface mode. The internal surface undulates in phase with the bilayer surface in order to preserve the thickness of each monolayer, and the relaxation is driven by the membrane bending rigidity and tension and damped to the surrounding viscous medium. The relaxation frequency is written as

$$\omega_h(k) = \frac{(\gamma_s + 2\gamma_{fr} + \kappa_m k^2)ke^{-kd_0}}{2\eta} \tag{4.34}$$

When we ignore the contribution from the tension and the correction term of e^{-kd_0}, $\omega_h(k)$ is equivalent to the standard hydrodynamic model of a thin elastic sheet (eq. (4.11)), which is plotted in Figure 4.7.

The second mode is a pure peristaltic dynamic mode describing undulations in the bilayer where the thickness of the monolayers undulates in phase (thickness fluctuations). The relaxation frequency is calculated as

$$\omega_u(k) = \frac{kK_A}{\eta_m k + 2\eta} = \frac{kK_A}{\eta(l_{SD}k + 2)} \tag{4.35}$$

The thickness fluctuation mode is driven by the area compressibility, K_A, and damped by the solvent and membrane monolayer viscosity, η and η_m, respectively. The mode is split into two regimes based on the Saffman–Delbrück length $l_{SD} = \eta_m/\eta$ [55]. The dissipation of the long wavelength modes, $kl_{SD} \ll 1$, is dominated by the solvent viscosity, while the short wavelength modes, $kl_{SD} \gg 1$, dissipate through the membrane viscosity. The relaxation frequency for the short wavelength modes can be written as $\omega_u \simeq K_A/\eta_m$. This expression suggests that the peristaltic mode can be seen as a local mode in the short wavelength limit, which is similar to the short wavelength behavior of the slipping mode $\omega_1(k)$ in the case where it is damped by the monolayer surface viscosity (see Figure 4.7) [102].

Finally, a dispersion relation for the movement of the internal membrane surface ($s(\vec{r})$ in Figure 4.8) gives the relaxation frequency

$$\omega_s(k) = \frac{K_A k^2(k^2 d_0^2 - 1)}{\eta(2k + k^2 l_{SD} + 2l_{SD}/l_r^2)} \tag{4.36}$$

The internal surface mode also is driven by the area compressibility; however, it dissipates through the inter-monolayer friction as well as through the solvent and membrane viscosities. The new length scale $l_r = \sqrt{\eta_m/b}$ represents the dimension at which the forces from the membrane viscosity and the inter-monolayer friction balance. This length scale was estimated to be $l_r \sim 10$ nm [53], which is much shorter than l_{SD}.

While the dispersion relations developed by Bingham, Smye, and Olmsted have not yet been incorporated into the expressions for $I(Q,t)$, they nevertheless provide important insights into the dynamics measured with NSE. As we will see in Section 4.4.2, these theories have begun to help link the phenomenologically measured thickness fluctuation timescale back to the inherent membrane elastic and viscous properties.

4.3.4 Comparing the dynamics predicted by different membrane models

In the past three subsections, the description of a biomembrane has evolved from a thin, structureless sheet (Section 4.3.1) to two coupled monolayers (Section 4.3.2) to a "thick" membrane that can undergo fluctuations in thickness as well as bending undulations (Section 4.3.3). With each section, both the illustrations and equations to describe the membrane dynamics have become more complicated as more terms are needed to describe the added contributions. To summarize the different theories, we compare the predicted dispersion relations in Figure 4.7. The following parameters were used to calculate the dispersion relations: $\kappa = 8.5\times10^{-20}$ J, $\eta = 8.7\times10^{-3}$ Pa·s, $\eta_m = 1\times10^{-9}$ Pa·s·m, $b = 1\times10^{7}$ Pa·s/m, $K_A = 12\kappa_m/d_0^2$, $\kappa = 2\kappa_m$, $d_t = 2d_0$, $d_t = 2.42\times10^{-9}$ m, and $\beta = 24$, where d_t and β are the hydrocarbon thickness of the bilayer and intermonolayer coupling constant, respectively, which will be introduced in Section 4.4.1.

Single membrane fluctuations: The solid gray line plots $\omega(k)$ versus the undulation mode wavenumber predicted from the standard hydrodynamic mode analysis based on the Helfrich bending Hamiltonian (eq. (4.11)). This model predicts a single dispersion relation across the entire fluctuation spectrum.

Two coupled monolayers: Incorporating the effects of inter-monolayer friction introduces a second dissipation mechanism. The modification of the Zilman and Granek (ZG) theory by Watson and Brown (WB) considered the change in the dispersion relation given by eq. (4.11) to incorporate the effects of inter-monolayer friction by replacing κ with $\tilde{\kappa}$. The dispersion relation predicted by WB is shown as the green dash-dotted line marked as $\omega_m(k) = \tilde{\kappa}k^3/4\eta$. $\omega_m(k)$ relaxes faster than $\omega(k)$ because the membrane is effectively stiffer with $\tilde{\kappa} > \kappa$.

WB applied the model developed by Seifert and Langer (SL) to the short wavelength fluctuations measured by NSE. The SL model gives two eigenvalues

for the dynamic modes of coupled monolayers, which are shown in red-dashed (ω_1) and dashed-solid (ω_2) lines. The main dissipation mechanism changes from $\omega_1(k)$ at long wavelengths ($k \ll k_1$) to $\omega_2(k)$ at short wavelengths ($k_1 \ll k$). At short wavelengths, $\omega_2(k)$ corresponds to the bending modes that are affected by the inter-monolayer friction and the fluctuations are governed by the effective bending modulus $\tilde{\kappa}$ also used by WB, so $\omega_2(k) = \omega_m(k)$. Meanwhile at long wavelengths, $\omega_1(k)$ corresponds to the hydrodynamically damped bending modes also predicted by Helfrich and $\omega_1(k) = \omega(k)$ at $k \ll k_1$.

Between the crossover wavenumbers, $k_1 < k < k_2$, $\omega_1(k)$ is determined by the slipping mode and then plateaus at high $k \gg k_2$ where the mode dissipates through the surface viscosity and is independent of wavenumber. However, for the chosen parameters, $k_1 < k < k_2$ range is quite narrow and the slipping mode does not contribute significantly despite its predicted importance by SL. The minor contribution of the slipping mode is due to the choice of η_m as well as b values used to calculate the dispersion relations in Figure 4.7. The experiments by Arriaga and colleagues found a b value that is much larger than the typical value used here ($b \sim 10^9$ Pa·s/m) [124], suggesting more thorough studies, combining experiment, simulation and theory, are needed to better understand inter-monolayer friction and how it affects the membrane dispersion relations.

"Thick" bilayers: The dispersion relation predicted by the model for "thick" membranes by Bingham, Smye, and Olmsted (BSO) are summarized by the blue-dashed (ω_h and ω_s) and dash-dotted (ω_u) lines. In the calculation, we neglected the contributions from the membrane tension ($\gamma_s = \gamma_{fr} = 0$) and plot only the contribution from the height fluctuation as $\omega_h(k)$. As such $\omega_h(k)$ completely overlaps with $\omega(k)$ from the Helfrich description. The thickness fluctuations ($\omega_u(k)$) are the fastest mode at low k, but plateau to an almost constant value above $k_{SD} \equiv 2\pi/l_{SD}$, the same behavior seen in the slipping mode of the SL model $\omega_1(k)$. The internal surface mode $\omega_s(k)$ also converges to the $\omega_u(k)$ in the high k range.

Now that we have covered the theory needed to describe the membrane undulations, we will see in the next section how it is applied to actual NSE data. As discussed in Section 4.2, NSE measures the spatial and time correlation function as $I(Q, t)$ on the nanometer and nanosecond scales and is thus uniquely suited to probing the small wavelength dynamics predicted to occur from 0.1 nm^{-1} to ~10 nm^{-1} in Q and from 1 ps to sub μs in t (10^8 $m^{-1} < Q < 10^{10}$ m^{-1} and 10^{-12} s $< t < 10^{-6}$ s). As we move into the next section, we remind the reader that NSE measures the scatterer's Q, which corresponds to the scattering vector and not the dynamic mode number which we call k here, though the experimentally measured length scales should be weighted in the corresponding k ranges.

4.4 Dynamics measurements

Having covered the theory on membrane dynamics and how NSE works, we now turn our attention to the design of an appropriate experimental system to which these methods and theories can be applied. While there are many model systems for lipid bilayers, most NSE experiments use large unilamellar vesicles (LUVs). Multilamellar vesicles (MLVs) have a strong correlation peak at $Q \approx 1\,nm^{-1}$ from the inter-layer spacing [147, 148]. The width of the Bragg peak measured in an elastic scattering technique such as small angle X-ray or neutron scattering (SAXS or SANS) can be used to determine the so-called Caillé parameter that is related to the membrane bending rigidity [149, 150]. However, in a quasi-elastic scattering technique like NSE, Bragg peaks result in a phenomenon known as de Gennes narrowing, in which the measured dynamics markedly slow down at the peak position [151]. Indeed, while Seto et al. were able to obtain an estimate of the bending modulus of multilamellar vesicles using NSE, the data deviated from the predicted Q^3 scaling due to the close proximity of the Bragg reflection [129]. It is therefore best to use unilamellar vesicles to measure membrane fluctuations and determine the membrane's mechanical properties. While MLVs are not ideal for NSE experiments, measurements can be made using aligned multilayers [81, 120, 152]. Note that these experiments will probe the dynamics parallel to the membrane plane in eq. (4.17), which we explicitly do not cover in this chapter.

Giant unilamellar vesicles (GUVs) are widely used as model systems to determine the membrane elastic properties by other methods, either through fluctuation analysis or micro-manipulation techniques [153, 154]. GUVs are microns in diameter, making them ideal for studying by light microscopy methods, but it also means they are quite dilute in solution. If we assume a GUV diameter of roughly 10 μm and the highest achievable packing fraction in solution to be 74% (assuming face-centered cubic, FCC, packing), the lipid concentration in solution would only be 0.17% by volume or about 2 mg/mL lipid in solution. Unfortunately this concentration range is much too small for neutron scattering experiments (especially for measuring dynamics) and we need to increase the amount of lipid in the sample to gain sufficient scattering intensities. Using LUVs with a diameter of ≈ 100 nm, the lipid concentration can be as high as 17%, assuming an FCC packing of vesicle in solution (about 200 mg/mL lipid in the solution), which gives enough scattering intensities for our purposes. Therefore, most NSE experiments use LUVs with diameters ranging from 30 to 200 nm. These vesicles are usually obtained by the extrusion method [153], where aqueous lipid solutions are pushed through a polycarbonate filter yielding relatively monodisperse vesicles whose diameter are determined by the filter pore size.

4.4.1 Bending fluctuations

Now that we have an experimental system, we will cover actual NSE data. Figure 4.9 shows a typical $I(Q,t)/I(Q,0)$ measured using NSE. The solid lines in Figure 4.9 are fits to a single membrane fluctuation model proposed by Zilman and Granek: eq. (4.20) [99, 113]. The first application of ZG theory to NSE data appeared in Takeda's paper in which they studied dipalmitoyl-phosphocholine (DPPC) lipid dispersed in D_2O with $CaCl_2$ [127]. While this lipid/salt mixture is multilamellar, no strong correlation peak was seen in the NSE data and the relaxation rate followed the Q^3 scaling predicted by Zilman and Granek [127]. Subsequent NSE studies on the same system were used to probe the bending dynamics in the fluid and gel phases to estimate the steric interactions between the bilayers in the unbound state [156].

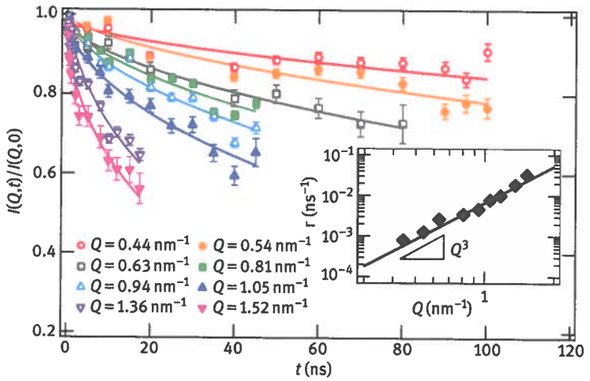

Figure 4.9: Normalized intermediate scattering function $I(Q,t)/I(Q,0)$ measured by NSE for protiated DMPC in D_2O at $T = 35\,^{\circ}C$. Inset indicates the Q-dependence of the relaxation rate Γ ($\propto Q^3$). Error bars represent ±1 standard deviation throughout the chapter.

Following the early studies of large unilamellar vesicles by Yi et al. [130], NSE has been used to study a wide range of lipid systems including the effects of fatty acyl tail structure [130, 157, 158], inclusion of small molecules such as cholesterol [159, 160], peptides [135, 161], drugs [83, 162–164], and nanoparticles [165], as well as the internal membrane fluctuations [58, 59, 166, 167]. Recently, NSE has also been used to measure more complex systems such as membrane domains [168] and more biologically relevant systems [169, 170].

The inset in Figure 4.9 shows Γ following a Q^3 dependence as expected from the expression for $\Gamma_{ZG_{mod}}$ given in eq. (4.28) with a slope that is proportional to $\tilde{\kappa}$. In Section 4.3.2, the effective bending modulus is given by $\tilde{\kappa} = \kappa + 2d_n^2 K_A$. Again, K_A is the *monolayer* area compressibility modulus and can be calculated as $K_A = 12\kappa_m/d_c^2$, where κ_m is the monolayer bending modulus and d_c is the monolayer hydrocarbon thickness [171]. The monolayer bending modulus is half the bilayer bending modulus, $\kappa_m = \kappa/2$, which means we can rewrite the expression for $\tilde{\kappa}$ in terms of the bilayer properties as $\tilde{\kappa} = \left\{1 + 48(d_n/2d_c)^2\right\}\kappa$. The remaining unknown in the expression for $\tilde{\kappa}$ is $d_n/2d_c$, the ratio of the neutral surface to the thickness of the hydrocarbon tails in the bilayer. Remember from Section 4.3.2, the neutral surface is defined as the surface at which the monolayer bending and stretching energies are decoupled and cannot be measured experimentally [45]. Generally, d_n is assumed to lie somewhere between half and the full monolayer thickness with corresponding values of $d_n/2d_c$ ranging from 0.25 to 0.6 [108, 135, 172–175]. The first NSE studies to use the Watson and Brown's equations to analyze NSE data used a value of $d_n/2d_c \approx 0.6$; which puts the neutral surface within the headgroup region of the bilayer [58, 59, 135]. d_n is generally thought to be closer to the interface between the lipid headgroups and tail, with $d_n/2d_c = 0.5$ [176–183]. Putting this value into the expression for $\tilde{\kappa}$ gives $\tilde{\kappa} = 13\kappa$, which shows how much more energy is required to bend the membrane at the NSE scales.

Having an expression for $\tilde{\kappa}$ in terms of the intrinsic bending modulus, $\Gamma_{ZG_{mod}}$ in eq. (4.28) can now be rewritten as [184]

$$\frac{\Gamma_{ZG_{mod}}}{Q^3} = 0.0069\sqrt{\frac{k_BT}{\kappa}}\frac{k_BT}{\eta}. \tag{4.37}$$

Therefore, we can determine the bilayer bending modulus κ from a plot of $\Gamma_{ZG_{mod}}$ versus Q measured in an NSE experiment. Note that changing the value of d_n only changes the numerical prefactor in eq. (4.37) and scales the value of κ by a constant.

Table 4.1 compares values of the bending modulus for DMPC bilayers at a temperature of about 30 °C measured with different experimental techniques. A similar comparison for POPC bilayers is presented in [73] and several other lipids in [185]. All values are on the order of 10 k_BT, but can vary significantly depending on the experimental technique. The NSE result is comparable to values determined from fluctuation analysis by Méléard et al. [186] and some computer simulations [175, 185], but differs by almost a factor of 3 with results obtained from other methods such as micropipette aspiration. Nagle and coworkers discussed the discrepancy between κ values measured by different techniques in detail in their recent work [187]. One important difference is that the different techniques measure the bending modulus on different length and timescales, so it is possible that there are other contributions

Table 4.1: Comparison of the bending modulus κ of DMPC bilayers at $T \approx 30\,^{\circ}C$ for various experimental and simulation techniques in literature.

Technique	T (°C)	κ (k_BT)
Neutron spin echo	**30**	35.6 ± 2.0 [184]
Fluctuation analysis	**30**	31.1 ± 1.9 [186]
Micropipette aspiration	**29**	13.4 ± 1.4 [153]
Diffuse x-ray scattering		
with tilt	**30**	24.6 ± 1 [112]
without tilt		15.6 ± 0.6 [112]
Computer Simulation	**30**	34.7 ± 1.2 [185]
		29.3 [175]

to the intrinsic membrane rigidity that are not captured by current theories described in Section 4.3.

As the bilayer bends, one leaflet must stretch while the other compresses. This physical relationship is expressed mathematically in a model for thin elastic sheets as $K_{A_b} = \beta\kappa/(2d_c)^2$ in which K_{A_b} is the *bilayer* area compressibility modulus [171]. The constant β depends on the degree of coupling between the two leaflets: $\beta = 12$ when the two monolayers are fully coupled and the bilayer behaves as a single slab, while $\beta = 48$ when the monolayers are completely uncoupled. Rawicz et al. proposed an intermediate value for lipid bilayers of $\beta = 24$ based on a polymer brush model [188]. Their model assumes that K_{A_b} is related to the bilayer surface pressure, Π, through a constant factor, $K_{A_b} = 6\Pi$, and that the surface pressure is dominated by the entropic contributions from the hydrocarbon tails which are modeled as idealized freely jointed polymer chains (hence the name polymer-brush model) [188]. Any contributions from interactions between the hydrocarbon tails and/or lipid headgroups are neglected, yet despite its simplicity, this model has been shown to hold true for a number of different lipid systems [189]. Because of its success in describing fluid lipid membranes, the polymer brush model is used regularly to relate a measured K_{A_b} to κ and vice versa.

Combining the κ values measured with NSE and d_c values that are measured with an elastic scattering technique such as SANS, we can now use the polymer brush model to calculate values for K_{A_b}. Figure 4.10 shows the resulting values for three phospholipids with different tail lengths and the same headgroup, dimyristoyl-, dipalmitoyl-, and distearoyl-phosphocholine (DMPC, DPPC, and DSPC) [184]. The values of K_{A_b} are independent of the lipid tail length as expected [188] and decrease with increasing temperature.

Here, we should note that the value of β from the polymer brush model may have some connection with the inter-monolayer friction constant b that appeared in the SL and BSO models. However, b did not contribute significantly to the

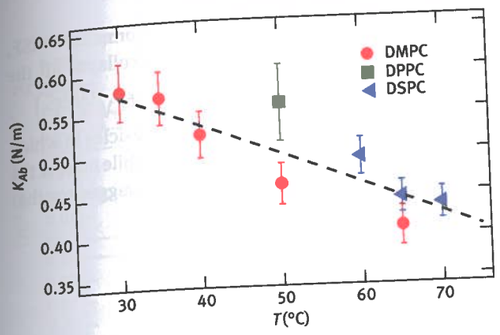

Figure 4.10: Temperature dependence of the bilayer area compressibility modulus K_{A_b} calculated from the values of κ estimated by NSE by adopting the polymer brush theory [188] to relate κ and K_{A_b} by $K_{A_b} = 24\kappa/(2d_c)^2$. The data are adapted with permission from [184]. Copyright 2017 American Chemical Society.

bending mode in these theories. Instead, b appeared in the slipping mode ($\omega_2(k)$) at small k. These small k values are not easy to access using NSE and are likely too fast to observe for DLS. Therefore, it is hard to determine if and how b and β are related. But, if we can independently measure κ and K_{A_b}, then, we can start to calculate the value of β and improve our understanding of both the dispersion relation and b.

4.4.2 Thickness fluctuations

We saw in the BSO model that, in addition to the bending fluctuations we measured in Section 4.4.1, membranes can also undergo thickness fluctuations. To measure the thickness fluctuations with NSE, we take advantage of a unique feature of neutron scattering that the scattering power of different isotopes can be vastly different. In particular, by judiciously replacing H with D, we can carefully control or even eliminate contrast, a technique known as contrast matching, without significantly modifying the properties of the sample. Thus by exchanging H for D in the lipid tails, the scattering contrast of the tails can be "matched" to the surrounding solvent, making the tails "invisible" to the neutrons and thus highlighting the scattering from the lipid headgroups. With this contrast condition, we now emphasize the dynamics from the headgroups and their relative motions.

Recalling the discussion in the previous section, we note that eqs. (4.21) and (4.28) indicate that the undulation fluctuations of a membrane follow a simple

scaling law. Thus, plotting the natural logarithm of the normalized ISF, $\ln[I(Q,t)/I(Q,0)]$ against $(Q^3t)^{2/3}$, as done in Figure 4.11, should collapse all the data onto a single master curve whose slope is given by $P = \left(0.0069\sqrt{\frac{k_BT}{\kappa}}\frac{k_BT}{\eta}\right)^{2/3}$. Figure 4.11 shows such a plot of NSE data for tail-deuterated DPPC vesicles in which the hydrocarbon tails are contrast-matched to the D_2O solvent [58]. While most of the data do follow the expected scaling, the data at $Q \approx 1.0\ \mathrm{nm}^{-1}$ do not, suggesting that there is another, faster relaxation process contributing at this Q.

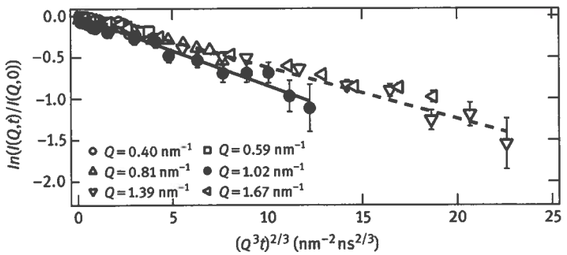

Figure 4.11: A single membrane undulation scaling plot of $\ln[I(Q,t)/I(Q,0)]$ vs $(Q^3t)^{2/3}$ for tail deuterated DPPC at $T = 50\,^{\circ}C$ suggested by eq. (4.28) [113]. All the data, except that for $Q = 1.02\ \mathrm{nm}^{-1}$, collapse onto a single line. Deviation of the data at $Q = 1.02\ \mathrm{nm}^{-1}$ from the undulation fluctuation scaling behavior supports the idea of an additional dynamic contribution at this specific Q.

As suggested by eq. (4.37), the enhanced dynamics can also be emphasized by plotting the data as Γ/Q^3 versus Q which, following the same scaling arguments above for pure undulation dynamics, leads to a horizontal line whose intercept is related to the bending modulus. The data for DMPC, DPPC, and DSPC bilayers plotted in this fashion in Figure 4.12 all show a distinct peak [58]. The deviation for all of the bilayers is very localized at Q around $1\ \mathrm{nm}^{-1}$ (length scales of ≈ 3 nm) which we assign to the membrane thickness fluctuations. The Q-value of the peak corresponds to the minimum in the scattered intensity of the membrane form factor measured in SANS, supporting the idea that the excess dynamics are occurring at the length scale of the membrane thickness. The same signature of membrane thickness fluctuations was also seen in NSE data for oil-swollen surfactant bilayers [141, 144, 145, 190]. The peak shift to lower Q from DMPC to DPPC to DSPC in Figure 4.12 then reflects the increase in bilayer thickness with increasing tail length. Note that these thickness fluctuations are only seen in the fluid phase of the membrane [58]. The peak in the data disappears at low temperatures below T_m (see Figure 4.12) when the lipids are in the gel phase and the membrane is more rigid and less dynamic.

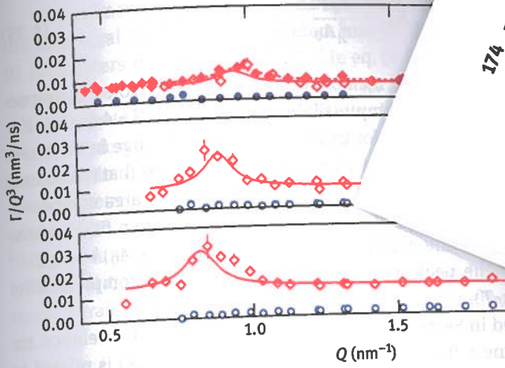

Figure 4.12: The relaxation rate measured by NSE is plotted in terms of Γ/Q^3 against Q. If the dynamics are solely undulation fluctuations, the value of Γ/Q^3 is flat as it is observed below the transition temperature T_m for each lipid. On the other hand, at $T > T_m$ a peak like enhancement is observed indicative of thickness fluctuations. The solid lines are the fit results according to eq. (4.38). Open and full symbols indicate the data collected on the NG5-NSE and IN15, respectively. The data are adapted with permission from [58]. Copyright 2012 The American Physical Society.

In order to further characterize the excess dynamics at the membrane thickness length scale, we assume that they can be captured by a simple additive term to the bending fluctuation decay rate given by eq. (4.37) and can be expressed by the following equation [144]

$$\frac{\Gamma}{Q^3} = \frac{\Gamma_{ZG_{mod}}}{Q^3} + \frac{\Gamma_{TF}}{Q_0^3}\frac{1}{1+(Q-Q_0)^2\xi^2}, \tag{4.38}$$

in which the first term describes the underlying bending dynamics, quantified using protiated lipid bilayers, and the second term empirically fits the thickness fluctuation peak. The two important parameters extracted from the Lorentz function are the relaxation time given by the decay constant $\tau_{TF} = 1/\Gamma_{TF}$ and the fluctuation amplitude $\Delta d_c = 2d_c(Q_0\xi)^{-1}$, which is given by the half width at half maximum of the Lorentzian, ξ^{-1} [141, 146, 191].

Earlier in the chapter, we noted that the characteristic length and timescales of the thickness fluctuations were related to the membrane's elastic and viscous properties, suggesting eq. (4.38) can be rewritten in terms of the intrinsic membrane properties.

Statistical mechanics predicts a relationship between the bilayer area compressibility modulus K_{A_b} and the fractional change in area $\sigma_A = \Delta A/A$ as [52, 192]

$$K_{A_b} = \frac{k_B T}{\sigma_A^2 A_0} \tag{4.39}$$

Where A and A_0 are the unit area of the membrane and the area per molecule, respectively. Assuming the bilayer volume compressibility is negligible ($V = Ad_c$, $\Delta V/V = \Delta A/A + \Delta d_c/d_c \approx 0$), σ_A is compensated for by a corresponding change in thickness $\sigma_d = \Delta d_c/d_c$, that is, $\sigma_d^2 = \sigma_A^2$. (Both simulation and experiment suggest that the volume compressibility is at least an order of magnitude smaller than the area compressibility, supporting that the assumption of $\Delta V/V \approx 0$ is reasonable to a first approximation [52, 193].) Therefore, the relation $\sigma_d^2 = (\Delta d/d)^2 = k_B T/(K_{A_b} A_0) = 4(Q_0\xi)^{-2}$ leads to an expression for the peak width in terms of the bilayer compressibility modulus $\xi^2 = 4K_{A_b}A_0/(Q_0^2 k_B T)$.

The BSO model covered in Section 4.3.3 [53] developed a dispersion relation for the peristaltic mode (thickness fluctuations), $\omega_u(k)$ in eq. (4.35). $\omega_u(k)$ is related to K_{A_b} and damped by the viscosities of the solvent, η, and membrane, η_m. When the wavelengths of the mode are shorter than the Saffman–Delbrück length [55], $l_{SD} = \eta_m/\eta$, the in-plane monolayer viscosity dominates and the damping is independent of the fluctuation wavelength. In general, this condition is satisfied in pure lipid bilayers as can be seen in Figure 4.7, and we can use the dispersion relation from the BSO model to relate the experimentally measured τ_{TF} to the membrane viscosity as [53]

$$\tau_{TF} \approx \frac{\eta_m}{K_{A_b}}. \tag{4.40}$$

These refinements lead to an expression for the Lorentzian based on the bilayer's elastic and viscous properties as [184]

$$\frac{\Gamma}{Q^3} = \frac{\Gamma_{ZG_{mod}}}{Q^3} + \frac{K_{A_b} k_B T}{\eta_m Q_0^3 k_B T + 4\eta_m Q_0 K_{A_b} A_0 (Q - Q_0)^2}. \tag{4.41}$$

In this equation, K_{A_b} is calculated from κ determined by NSE experiments with protiated lipid bilayers using the polymer brush model, $K_{A_b} = 24\kappa/(2d_c)^2$ and assuming that K_{A_b} is the same for protiated and tail-deuterated lipids within the experimental uncertainty. The area per lipid is given by $A_0 = V_L/(d_c + d_h)$, where V_L and d_h represent the lipid volume and the headgroup thickness, respectively. V_L can be determined from density measurement to find the specific molecular volume [194] or calculated from equations for the lipid volume available in literature [195]. The tail thickness can be determined from an elastic small angle scattering experiment (such as SANS or SAXS), and the headgroup thickness, while not yet well defined, is generally assumed to be on the order of $d_h = 1$ nm [196–198]. Q_0 can also be determined from a SANS or diffraction measurement. Thus, all the parameters in eq. (4.41) are known except for the membrane viscosity η_m.

The refined analysis method now defines the peak shape in Γ/Q^3 in terms of the structural and elastic parameters and in the process reduced the number of fit parameters from two (τ_{TF} and ξ^{-1} in eq. (4.38)) to one (η_m in eq. (4.41)). Based on eq. (4.41), the peak width is related to K_{A_b}; however, experimentally the data also contain effects from the instrumental Q resolution. The Q resolution smearing can be taken into account using the expressions developed for SANS instruments [199], and the resolution function can be convoluted with eq. (4.41) to fit the NSE data. The fit result is plotted in Figure 4.13 for the temperature variation of Γ/Q^3 in the fluid phase of the DMPC vesicles in which the instrumental Q resolution was expressed as a Gaussian function with a full width at half maximum of ≈ 13% [184]. Note that the baseline at $Q > Q_0$ does not capture the experimental data, which suggests that additional intramembrane dynamics may be present that are not currently considered.

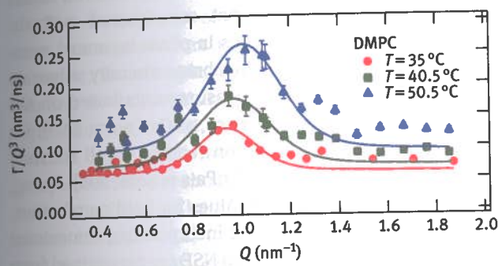

Figure 4.13: Temperature variation of Γ/Q^3 against Q for DMPC membranes is shown together with the fit results according to eq. (4.41) using a single fit parameter: the membrane viscosity η_m. The instrumental Q resolution is also accounted for in the fit. Reprinted with permission from [184]. Copyright 2017 American Chemical Society.

Reformulating the expression for the bilayer thickness fluctuations in terms of the membrane properties now allows us to determine the membrane viscosity η_m from the NSE data. The temperature dependence of η_m determined from NSE measurements is shown in Figure 4.14 for DMPC, DPPC, and DSPC [184]. The estimated values of η_m are on the order of 10 nPa·s·m, and increase with increasing tail length and decreasing temperature, which qualitatively matches the trends seen in linear alkanes [200, 201]. Interestingly, the measured η_m values for these three lipids are about the same ($\eta_m \approx 100$ nPa·s·m) at $T \approx T_m$ and decrease by as much as a factor of 2 with increasing temperature, which suggests a strong coupling between the bilayer phase behavior and the lipid motion.

Reported values for the membrane viscosity in literature vary widely. While some of the discrepancies may be due to differences in studied temperatures, the temperature

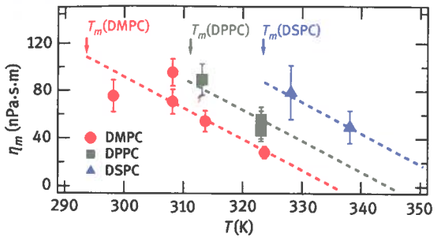

Figure 4.14: The membrane viscosity η_m calculated from the NSE result. The dashed straight lines are guide the eyes. Reprinted with permission from [184]. Copyright 2017 American Chemical Society.

variation seen in Figure 4.14 over a 50 K range does not account for the two orders of magnitude variations seen in literature with different experimental methods. Fluorescent probe measurements, tracking domain motions in phase separated membranes, and falling ball viscometry measurements give membrane viscosity values on the order of ($\approx$ 2 to 3) nPa·s·m [183, 202–206] while measurements based on the diffusion of tracer particles give viscosities on the order of $\approx$ 10 nPa·s·m [207]. On the other hand, membrane viscosities estimated based on red blood cell recovery times in micropipette aspiration measurements are $\approx$ 700 nPa·s·m [208, 209]. The η_m values from NSE fall within the wide range of reported values for lipid membranes, and perhaps more importantly, were determined without incorporating fluorescent probes or tracer particles. Instead, the viscosity values from NSE are determined from the relaxation timescales of the naturally occurring membrane fluctuations. Similar NSE experiments were also used to determine the viscosity of oil-swollen surfactant membranes [190]. In this case, the η_m determined from NSE could be compared with the measured bulk viscosity of the oil-surfactant mixtures η_s as $\eta_m = d_m\eta_s$ with d_m as the membrane thickness. Both measurements gave similar values of η_m further supporting the utility of NSE to also determine the viscosity of membrane systems.

4.5 Summary and future perspective

In this chapter, we presented the observation of collective membrane fluctuations with NSE and the theory needed to relate the measured dynamics to the membrane elastic and viscous properties. By measuring the bending and thickness fluctuations on the nanoscale, we can independently determine the bilayer bending modulus, κ, area compressibility modulus, K_{A_b}, and monolayer viscosity, η_m. These same properties that govern the equilibrium thermal fluctuations will also influence the membrane's viscoelastic response to nonequilibrium deformations that are an essential

part of cell function as they package cargo, shape organelles and respond to external forces that we talked about at the beginning of the chapter [210]. Measuring both the bending and thickness fluctuations with NSE also opens the possibility of determining the inter-monolayer coupling constant β. While extracting an independent determination of K_{A_b} from the thickness fluctuation measurements is currently limited by the quality of the experimental data, continued improvement in NSE instrumentation and data analysis may make these measurements more robust in the future. Alternatively, β could be determined by combining NSE with another technique to measure κ or K_{A_b}, such as those outlined in other chapters of this book. Gelation [211], degree of saturation of the lipid tail [212], and mixing lipids with cholesterol [189] are all known to modulate inter-monolayer coupling and the NSE measurements described here can be used to not only gain insights into a wide variety of lipid bilayers, but help advance our understanding of the complex dissipation mechanisms in these systems.

The development of theory and experiment go hand-in-hand, and extracting more information from the NSE measurements requires a solid theoretical basis. Currently, for example, the thickness fluctuations are treated as an excess to the bending fluctuations and assumed to be an additive term in the decay constant expression (eq. (4.41)), and the $I(Q,t)$ data are fit using the stretched exponential function of the single membrane fluctuation model. In principle though, these two independent modes should be treated as two individual relaxations in $I(Q,t)$. Just as Mell and colleagues have developed a relaxation function incorporating the hybrid modes (Section 4.3.2) [125], proper data treatment for the thickness fluctuations requires the correct relaxation function for $I(Q,t)$ to understand the relaxation behavior and dispersion relation of this dynamic mode.

Recent theory, simulation and experimental works have also begun to incorporate tilt degrees of freedom, described by a tilt modulus, into the analysis of the nanoscale dynamics. The tilt modulus introduces another parameter, in addition to the bending and thickness fluctuation parameters, and these models now have literally too many parameters (see, e.g., Table II in Ref. [108]) to reliably extract from a single experimental measurement. Quantifying all of the lipid membrane properties will require combining multiple experimental techniques with the appropriate theories. For example, recent development of diffuse X-ray scattering allows one to determine both the bending and tilt moduli [109, 112, 213, 214], which could be combined with NSE measurements. The length and timescales probed by scattering methods in particular are highly complementary to ranges accessible by computer simulation, even for thickness fluctuations [141, 146], and combining simulation and experiment is a powerful opportunity to probe the complexities of membrane dynamics.

The theoretical and experimental framework outlined in this chapter provides a foundation for understanding the elastic and viscous properties of lipid membranes, and we hope the examples provided here inform and inspire ongoing investigations into more complex and biologically relevant systems. All of the example NSE data

shown in the chapter were for simple saturated lipid bilayers, yet a single cell membrane can contain hundreds of chemically distinct lipids. While we know this remarkable complexity is essential to cell function, our understanding of how it fundamentally affects the membrane properties is still developing. For example, decades of research have shown that the effects of cholesterol on the membrane properties are highly dependent on the lipid species and our picture of cholesterol-containing membranes is still evolving. Moreover, cell membranes are not only made of lipids, but can contain upwards of 50% by mass of proteins. Simply altering the thickness of model membranes has been shown to affect the biological activity of several proteins while incorporating peptides into lipid membranes also is known to affect the bilayer structural properties. Clearly, there is a synergy in lipid–protein interactions in determining the membrane properties; however, the nature of these interactions are not well understood. All of these intricacies relate to the synergy among structure, dynamics, and functions of biological membranes, and NSE is providing unique insights into the interdependence of the membrane collective dynamics and the elastic and viscous properties.

Acknowledgments

Access to the NGA-NSE was provided by the Center for High Resolution Neutron Scattering, a partnership between the National Institute of Standards and Technology and the National Science Foundation under Agreement No. DMR-1508249. The access to the IN15 was granted through the proposal No. 9-13-353. M.N. acknowledges funding support of cooperative agreement 70NANB15H259 from NIST, US Department of Commerce.

References

[1] Goetz, R., Gompper, G., & Lipowsky, R. Mobility and elasticity of self-assembled membranes. *Phys. Rev. Lett.*, 82:221–224, 1999.
[2] Klauda, J.B., Roberts, M.F., Redfield, A.G., Brooks, B.R., & Pastor, R.W. Rotation of lipids in membranes: Molecular dynamics simulation, ^{31}P spin-lattice relaxation, and rigid-body dynamics. *Biophys. J.*, 94:3074–3083, 2008.
[3] Vaz, W.L.C., Goodsaid-Zalduondo, F., & Jacobson, K. Lateral diffusion of lipids and proteins in bilayer membranes. *FEBS. Lett.*, 174:199–207, 1984.
[4] Almeida, P.F.F., & Vaz, W.L.C. *Handbook of Biological Physics, Volume I*, chapter 6 Lateral Diffusion in Membranes. Elsevier Science, Amsterdam, pp. 305–357, 1995.
[5] Singer, S.J., & Nicolson, G.L. The fluid mosaic model of the structure of cell membranes. *Science*, 175:720–731, 1972.

[6] Brown, D.A., & London, E. Functions of lipid rafts in biological membranes. *Annu. Rev. Cell Dev. Biol.*, 14:111–136, 1998.
[7] Engelman, D.M. Membranes are more mosaic than fluid. *Nature*, 438:578–580, 2005.
[8] McMahon, H.T., & Gallop, J.L. Membrane curvature and mechanisms of dynamic cell membrane remodelling. *Nature*, 438:590–596, 2005.
[9] McMahon, H.T., & Boucrot, E. Membrane curvature at a glance. *J. Cell. Sci.*, 128:1065–1070, 2015.
[10] Browicz, T. Further observation of motion phenomena on red blood cells in pathological states. *Zbl. Med. Wiss.*, 28:625–627, 1890.
[11] Turlier, H., Fedosov, D.A., Audoly, B., Auth, T., Gov, N.S., Sykes, C., Joanny, J.-F., Gompper, G., & Betz, T. Equilibrium physics breakdown reveals the active nature of red blood cell flickering. *Nat. Phys.*, 12:513–519, 2016.
[12] Helfrich, W. Elastic properties of lipid bilayers: Theory and possible experiments. *Z. Naturforsch.*, 28 c:693–703, 1973.
[13] Netz, R.R. Complete unbinding of fluid membranes in the presence of short-ranged forces. *Phys. Rev. E.*, 51:2286–2294, 1995.
[14] Marx, S., Schilling, J., Sackmann, E., & Bruinsma, R. Helfrich repulsions and dynamical phase separation of multicomponent lipid bilayers. *Phys. Rev. Lett.*, 88:138102, 2002.
[15] Dan, N., Pincus, P., & Safran, S.A. Membrane-induced interactions between inclusions. *Langmuir*, 9:2768–2771, 1993.
[16] Netz, R.R. Inclusions in fluctuating membranes: Exact results. *J. Phys. I France*, 7:833–852, 1997.
[17] Dean, D.S., Parsegian, V.A., & Podgornika, R. Fluctuation mediated interactions due to rigidity mismatch and their effect on miscibility of lipid mixtures in multicomponent membranes. *J. Phys.: Condens. Matter*, 27:214004, 2015.
[18] Maurya, S.R., Chaturvedi, D., & Mahalakshmi, R. Modulating lipid dynamics and membrane fluidity to drive rapid folding of a transmembrane barrel. *Sci. Rep.*, 3:1989, 2013.
[19] Huang, H.W. Deformation free energy of bilayer membrane and its effect on gramicidin channel lifetime. *Biophys. J.*, 50:1061–1070, 1986.
[20] Helfrich, P., & Jakobsson, E. Calculation of deformation energies and conformations in lipid membranes containing gramicidin channels. *Biophys. J.*, 57:1075–1084, 1990.
[21] Andersen, O.S., & Koeppe, R.E., II Bilayer thickness and membrane protein function: An energetic perspective. *Annu. Rev. Biophys. Biomol. Strut.*, 36:107–130, 2007.
[22] Phillips, R., Ursell T., Wiggins P., and Sens P. Emerging roles for lipids in shaping membrane-protein function. *Nature*, 459:379–385, 2009.
[23] Stevenson, P., & Tokmakoff, A. Time-resolved measurements of an ion channel conformational change driven by a membrane phase transition. *Proc. Natl. Acad. Sci.*, 114:10840–10845, 2017.
[24] Raudino, A., & Pannuzzo, M. Adhesion kinetics between a membrane and a flat substrate. An ideal upper bound to the spreading rate of an adhesive patch. *J. Phys. Chem. B.*, 114:15495–15505, 2010.
[25] Fenz, S.F., Bihr, T., Merkel, R., Seifert, U., Sengupta, K., & Smith, A.-S. Switching from ultraweak to strong adhesion. *Adv. Mater.*, 23:2622–2626, 2011.
[26] Bihr, T., Seifert, U., & Smith, A.-S. Nucleation of ligand-receptor domains in membrane adhesion. *Phys. Rev. Lett.*, 109:258101, 2012.
[27] Bihr, T., Seifert, U., & Smith, A.-S. Multiscale approaches to protein-mediated interactions between membranes - relating microscopic and macroscopic dynamics in radially growing adhesions. *New J. Phys.*, 17:083016, 2015.
[28] Fenz, S.F., Bihr, T., Schmidt, D., Merkel, R., Seifert, U., Sengupta, K., & Smith, A.-S. Membrane fluctuations mediate lateral interaction between cadherin bonds. *Nat. Phys.*, 13:906–913, 2017.

[29] Stachowiak, J.C., Brodsky, F.M., & Miller, E.A. A cost-benefit analysis of the physical mechanisms of membrane curvature. *Nat. Cell. Bio.*, 15:1019–1027, 2013.
[30] Zidovska, A., & Sackmann, E. Brownian motion of nucleated cell envelopes impedes adhesion. *Phys. Rev. Lett.*, 94:048103, 2006.
[31] Pierres, A., Benoliel, A.-M., Touchard, D., & Bongrand, P. How cells tiptoe on adhesive surfaces before sticking. *Biophys. J.*, 94:4114–4122, 2008.
[32] Biswas, A., Alex, A., & Sinha, B. Mapping cell membrane fluctuations reveals their active regulation and transient heterogeneities. *Biophys. J.*, 113:1768–1781, 2017.
[33] Pontes, B., Ayala, Y., Fonseca, A.C.C., Romão, L.F., Amaral, R.F., Salgado, L.T., Lima, F.R., Farina, M., Viana, N.B., Moura-Neto, V., & Nussenzveig, H.M. Membrane elastic properties and cell function. *PLOS One.*, 8:e67708, 2013.
[34] Monzel, C., Schmidt, D., Kleusch, C., Kirchenbücler, D., Seifert, U., Smith, A.-S., Sengupta, K., & Merkel, R. Measuring fast stochastic displacements of bio-membranes with dynamic optical displacement spectroscopy. *Nat. Commun.*, 6:8162, 2015.
[35] Cojoc, D., Finaurini, S., Livshits, P., Gur, E., Shapira, A., Mico, V., & Zalevsky, Z. Toward fast malaria detection by secondary speckle sensing microscopy. *Biomed. Opt. Express*, 3: 991–1005, 2012.
[36] Park, Y.-K., Diez-Silva, M., Popescu, G., Lykotrafitis, G., Choi, W., Feld, M.S., & Suresh, S. Refractive index maps and membrane dynamics of human red blood cells parasitized by *Plasmodium falciparum*. *Proc. Natl. Acad. Sci.*, 105:13730–13735, 2008.
[37] Shaked, N.T., Satterwhite, L.L., Telen, M.J., Truskey, G.A., & Wax, A. Quantitative microscopy and nanoscopy of sickle red blood cells performed by wide field digital interferometry. *J. Biomed. Opt.*, 16:030506, 2011.
[38] Yoon, Y.-Z., Hong, H., Brown, A., Kim, D.C., Kang, D.J., Lew, V.L., & Cicuta, P. Flickering analysis of erythrocyte mechanical properties: Dependence on oxygenation level, cell shape, and hydration level. *Biophys. J.*, 97:1606–1615, 2009.
[39] Byun, H., Hillman, T.R., Higgins, J.M., Diez-Silva, M., Peng, Z., Dao, M., Dasari, R.R., Suresh, S., & Park, Y. Optical measurements of biomechanical properties of individual erythrocytes from a sickle cell patient. *Acta Biomater.*, 8:4130–4138, 2012.
[40] Partin, A.W., Schoeniger, J.S., Mohler, J.L., & Coffey, D.S. Fourier analysis of cell motility: Correlation of motility with metastatic potential. *Proc. Natl. Acad. Sci.*, 86:1254–1258, 1989.
[41] Braig, S., Schmidt, B.U.S., Stoiber, K., Händel, C., Möhn, T., Werz, O., Müller, R., Zahler, S., Koeberle, A., Käs, J.A., & Vollmar, A.M. Pharmacological targeting of membrane rigidity: Implications on cancer cell migration and invasion. *New. J. Phys.*, 17:083007, 2015.
[42] Handel, C., Schmidt, B.U.S., Schiller, J., Dietrich, U., Mohn, T., Kiebling, T.R., Pawlizak, S., Fritsch, A.W., Horn, L.-R., Briest, S., Hockel, M., Zink, M., & Kas, J.A. Cell membrane softening in human breast and cervical cancer cells. *New J. Phys.*, 17:083007, 2015.
[43] Suezaki, Y., & Ichinose, H. A theory on the bending moduli of thin membranes by the use of a simple molecular model. *J. Phys. I France*, 5:1469–1480, 1995.
[44] Safran, S.A. *Statistical Thermodynamics of Surfaces, Interfaces, and Membranes*. Addison-Wesley, Massachusetts, 1994.
[45] Safran, S.A. Curvature elasticity of thin films. *Adv. Phys.*, 48(4):395–448, 1999.
[46] Hladky, S.B., & Gruen, D.W.R. Thickness fluctuations in black lipid membranes. *Biophys. J.*, 38:251–258, 1982.
[47] Miller, I.R. Energetics of fluctuation in lipid bilayer thickness. *Biophys. J.*, 45:643–644, 1984.
[48] Hladky, S.B., & Gruen, D.W.R. Response to energetics of fluctuation in lipid bilayer thickness by I. R. Miller. *Biophys. J.*, 45:645–646, 1984.

[49] Popescu, D., Ion, S., Popescu, A., & Movileanu, L. Elastic properties of bilayer lipid membranes and pore formation. In H.T. Tien and A. Ottova-Leitmannova, editors, *Planar Lipid Bilayers (BLMs) and Their Applications*, pages 173-204. Elsevier, Amsterdam 2003.
[50] Movileanu, L., Popescu, D., Ion, S., & Popescu, A.I. Transbilayer pores induced by thickness fluctuations. *Bull. Math. Biol.*, 68:1231–1255, 2006.
[51] Kaufmann, K., Hanke, W., & Corcia, A. *Ion Channel Fluctuations in Pure Lipid Bilayer Membranes: Control by Voltage*. Caruaru, Brazil, 1989.
[52] Lindahl, E., & Edholm, O. Mesoscopic undulations and thickness fluctuations in lipid bilayers from molecular dynamics simulations. *Biophys. J.*, 79:426–433, 2000.
[53] Bingham, R.J., Smye, S.W., & Olmsted, P.D. Dynamics of an asymmetric bilayer lipid membrane in a viscous solvent. *Europhys. Lett.*, 111:18004, 2015.
[54] Seifert, U. Configurations of fluid membranes and vesicles. *Adv. Phys.*, 46:13–137, 1997.
[55] Saffman, P.G., & Delbrück, M. Brownian motion in biological membranes. *Proc. Natl. Acad. Sci. USA.*, 72:3111–3113, 1975.
[56] Hughes, B.D., Pailthorpe, B.A., & White, L.R. The translational and rotational drag on a cylinder moving in a membrane. *J. Fluid Mech.*, 110:349–372, 1981.
[57] Petrov, E.P., & Schwille, P. Translational diffusion in lipid membranes beyond the Saffman-Delbrück approximation. *Biophys. J.*, 107:L41–L43, 2008.
[58] Woodka, A.C., Butler, P.D., Porcar, L., Farago, B., & Nagao, M. Lipid bilayers and membrane dynamics: Insight into thickness fluctuations. *Phys. Rev. Lett.*, 109:058102, 2012.
[59] Ashkar, R., Nagao, M., Butler, P.D., Woodka, A.C., Sen, M.K., & Koga, T. Tuning membrane thickness fluctuations in model lipid bilayers. *Biophys. J.*, 109:106–112, 2015.
[60] Seeling, A., & Seelig, J. Dynamic structure of fatty acyl chains in a phospholipid bilayer measured by deuterium magnetic resonance. *Biochemistry*, 13:4839–4845, 1974.
[61] Brown, M.F., Ribeiro, A.A., & Williams, G.D. New view of lipid bilayer dynamics from ^{2}H and ^{13}C NMR relaxation time measurements. *Proc. Natl. Acad. Sci. USA.*, 80: 4325–4329, 1983.
[62] Leftin, A., & Brown, M.F. An NMR database for simulations of membrane dynamics. *Biochim. Biophys. Acta Biomembr.*, 1808:818–839, 2011.
[63] Yellin, N., & Levin, I.W. Hydrocarbon chain trans-gauche isomerization in phospholipid bilayer gel assemblies. *Biochemistry*, 16:642–647, 1977.
[64] Wallach, D.F.H., Verma, S.P., & Fookson, J. Application of laser Raman and infrared spectroscopy to the analysis of membrane structure. *Biochim. Biophys. Acta*, 559:153–208, 1979.
[65] Pink, D.A., Green, T.J., & Chapman, D. Raman scattering in bilayers of saturated phosphatidylcholines. Experiment and theory. *Biochemistry*, 19:349–356, 1980.
[66] Mendelsohn, R., Davies, M.A., Brauner, J.W., Schuster, H.F., & Dluhy, R.A.. Quantitative determination of conformational disorder in the acyl chains of phospholipid bilayers by infrared spectroscopy. *Biochemistry*, 28:8934–8939, 1989.
[67] Klösgen, B., Reichle, C., Kohlsmann, S., & Kramer, K.D.. Dielectric spectroscopy as a sensor of membrane headgroup mobility and hydration. *Biophys. J.*, 71:3251–3260, 1996.
[68] Lange, A., Marsh, D., Wassmer, K.H., Meier, P., & Kothe, G. Electron spin resonance study of phospholipid membranes employing a comprehensive line-shape model. *Biochemistry*, 24:4383–4392, 1985.
[69] Marsh, D., & Horváth, L.I. Structure, dynamics and composition of the lipid-protein interface. Perspectives from spin-labelling. *Biochim. Biophys. Acta Rev. Biomembr.*, 1376:267–296, 1998.
[70] Subczynski, W.K., & Kusumi, A. Dynamics of raft molecules in the cell and artificial membranes: approaches by pulse EPR spin labeling and single molecule optical microscopy. *Biochim. Biophys. Acta*, 1610:231–243, 2003.

[71] Faucon, J.F., Mitov, M.D., Méléard, P., Bivas, I., & Bothorel, P. Bending elasticity and thermal fluctuations of lipid membranes. Theoretical and experimental requirements. *J. Phys. France*, 50:2389–2414, 1989.
[72] Mutz, M., & Helfrich, W. Bending rigidities of some biological model membranes as obtained from the Fourier analysis of contour sections. *J. Phys. France*, 51:991–1002, 1990.
[73] Dimova, R. Recent developments in the field of bending rigidity measurements on membranes. *Adv. Coll. Int. Sci.*, 208:225–234, 2014.
[74] Monzel, C., & Sengupta, K. Measuring shape fluctuations in biological membranes. *J. Phys. D.: Appl. Phys.*, 49:243002, 2016.
[75] Chadwick, J. Possible existence of a neutron. *Nature*, 129:312, 1932.
[76] Meyer, A., Dimeo, R.M., Gehring, P.M., & Neumann, D.A. The high flux backscattering spectrometer at the NIST Center for Neutron Research. *Rev. Sci. Instrum.*, 74:2759–2777, 2003.
[77] Copley, J.R.D., & Cook, J.C. The disk chopper spectrometer at NIST: a new instrument for quasielastic neutron scattering studies. *Chem. Phys.*, 292:477–485, 2003.
[78] Pfeiffer, W., Henkel, T., Sackmann, E., Knoll, W., & Richter, D. Local dynamics of lipid bilayers studied by incoherent quasi-elastic neutron scattering. *Europhys. Lett.*, 8:201–206, 1989.
[79] Armstrong, C.L., Kaye, M.D., Zamponi, M., Mamontov, E., Tyagi, M., Jenkins, T., & Rheinstädter, M.C. Diffusion in single supported lipid bilayers studied by quasi-elastic neutron scattering. *Soft Matter*, 6:5864–5867, 2010.
[80] Armstrong, C.L., Trapp, M., Peters, J., Seydel, T., & Rheinstädter, M.C. Short range ballistic motion in fluid lipid bilayers studied by quasi-elastic neutron scattering. *Soft Matter*, 7:8358–8362, 2011.
[81] Armstrong, C.L., Häußler, W., Seydel, T., Katsaras, J., & Rheinstädter, M.C. Nanosecond lipid dynamics in membranes containing cholesterol. *Soft Matter*, 10:2600–2611,2014.
[82] Sharma, V.K., Mamontov, E., Tyagi, M., Qian, S., Rai, D.K., & Urban, V.S. Dynamical and phase behavior of a phospholipid membrane altered by an antimicrobial peptide at low concentration. *J. Phys. Chem. Lett.*, 7:2394–2401, 2016.
[83] Sharma, V.K., Mamontov, E., Ohl, M., & Tyagi, M. Incorporation of aspirin modulates the dynamical and phase behavior of the phospholipid membrane. *Phys. Chem. Chem. Phys.*, 19:2514–2524, 2017.
[84] Yamada, T., Takahashi, N., Tominaga, T., Takata, S., & Seto, H. Dynamical behavior of hydration water molecules between phospholipid membranes. *J. Phys. Chem. B.*, 121:8322–8329, 2017.
[85] Mezei, F. Neutron spin echo: A new concept in polarized thermal neutron techniques. *Z. Physik.*, 255:146–160, 1972.
[86] Mezei, F. *Lecture Notes in Physics*, volume 128. Springer-Verlag, 1979.
[87] Farago, B., Falus, P., Hoffmann, I., Gradzielski, M., Thomas, F., & Gomez, C. The IN15 upgrade. *Neutron News.*, 26:15–17, 2015.
[88] Takeda, T., Komura, S., Seto, H., Nagai, M., Kobayashi, H., Yokoi, E., Zeyen, C.M.E., Ebisawa, T., Tasaki, S., Ito, Y., Takahashi, S., & Yoshizawa, H. A neutron spin echo spectrometer with two optimal field shape coils for neutron spin precession. *Nucl. Instrum. Meth. A.*, 364:186–192, 1995.
[89] Monkenbusch, M., Schätzler, R., & Richter, D. The Jülich neutron spin-echo spectrometer — Design and performance. *Nucl. Instrum. Meth. A.*, 399:301–323, 1997.
[90] Farago, B. Recent neutron spin-echo developments at the ILL (IN11 and IN15). *Physica B.*, 267–268:270–276, 1999.
[91] Rosov, N., Rathgeber, S., & Monkenbusch, M. Neutron spin echo spectroscopy at the NIST Center for Neutron Research. In P. Cebe, B. S. Hsaio, & D. J. Lohse, editors, *Scattering from polymers: characterization by x-rays, neutrons, and light*, pages 103–116. American Chemical Society: Washington D. C., 2000.

[92] Mezei, F. *Lecture Notes in Physics*, volume 601. Springer-Verlag Berlin Heidelberg, 2003.
[93] Nagao, M., Yamada, N.L., Kawabata, Y., Seto, H., Yoshizawa, H., & Takeda, T. Relocation and upgrade of neutron spin echo spectrometer, iNSE. *Physica B.*, 385–386:1118–1121, 2006.
[94] Holderer, O., Monkenbusch, M., Schätzler, R., Kleines, H., Westerhausen, W., & Richter, D. The JCNS neutron spin-echo spectrometer J-NSE at the FRM II. *Meas. Sci. Technol.*, 19:034022, 2008.
[95] Ohl, M., Monkenbusch, M., Arend, N., Kozielewski, T., Vehres, G., Tiemann, C., Butzek, M., Soltner, H., Giesen, U., Achten, R., Stelzer, H., Lindenau, B., Budwig, A., Kleines, H., Drochner, M., Kaemmerling, P., Wagener, M., Möller, R., Iverson, E.B., Sharp, M., & Richter, D. The spin-echo spectrometer at the spallation neutron source (SNS). *Nucl. Instrum. Meth. A.*, 696:85–99, 2012.
[96] Fouquet, P., Ehlers, G., Farago, B., Pappas, C., & Mezei, F. The wide-angle neutron spin echo spectrometer project WASP. *J. Neutron Res.*, 15:39–47, 2007.
[97] Häussler, W., Gohla-Neudecker, B., Schwikowski, R., Streibl, D., & Böni, P. RESEDA — The new resonance spin echo spectrometer using cold neutrons at the FRM-II. *Physica B.*, 397:112–114, 2007.
[98] Hino, M., Oda, T., Kitaguchi, M., Yamada, N.L., Sagehashi, H., Kawabata, Y., & Seto, H. Current status of BL06 beam line for VIN ROSE at J-PARC/MLF. *Phys. Procedia.*, 42:136–141, 2013.
[99] Zilman, A.G., & Granek, R. Membrane dynamics and structure factor. *Chem. Phys.*, 284: 195–204, 2002.
[100] Suezaki, Y. *Physics of Lipid Membranes [in Japanese]*. Kyushu University Publisher, Fukuoka, 2007.
[101] Yeung, A., & Evans, E. Unexpected dynamics in shape fluctuations of bilayer vesicles. *J. Phys. II France*, 5:1501–1523, 1995.
[102] Seifert, U., & Langer, S.A. Viscous modes of fluid bilayer membranes. *Europhys. Lett.*, 23: 71–76, 1993.
[103] Seifert, U., & Langer, S.A. Hydrodynamics of membranes: The bilayer aspect and adhesion. *Biophys. Chem.*, 49:13–22, 1994.
[104] Evans, E., & Needham, D. Physical properties of surfactant bilayer membranes: Thermal transitions, elasticity, rigidity, cohesion, and colloidal interactions. *J. Phys. Chem.*, 91: 4219–4228, 1987.
[105] Akabori, K., & Nagle, J.F. Structure of the DMPC lipid bilayer ripple phase. *Soft Matter*, 11: 918–926, 2015.
[106] Hamm, M., & Kozlov, M.M. Elastic energy of tilt and bending of fluid membranes. *Eur. Phys. J. E.*, 3:323–335, 2000.
[107] May, S., Kozlovsky, Y., Ben-Shaul, A., & Kozlov, M.M.. Tilt modulus of a lipd monolayer. *Eur. Phys. J. E.*, 14:299–308, 2004.
[108] Watson, M.C., Penev, E.S., Welch, P.M., & Brown, F.L.H. Thermal fluctuations in shape, thickness, and molecular orientation in lipid bilayers. *J. Chem. Phys.*, 135:244701, 2011.
[109] Jablin, M.S., Akabori, K., & Nagle, J.F. Experimental support for tilt-dependent theory of biomembrane mechanics. *Phys. Rev. Lett.*, 113:248102, 2014.
[110] Wang, X., & Deserno, M. Determining the lipid tilt modulus by simulating membrane buckles. *J. Phys. Chem. B.*, 120:6061–6073, 2016.
[111] Terzi, M.M., & Deserno, M. Novel tilt-curvature coupling in lipid membranes. *J. Chem. Phys.*, 147:084702, 2017.
[112] Nagle, J.F. Experimentally determined tilt and bending moduli of single-component lipid bilayers. *Chem. Phys. Lipids*, 205:18–24, 2017.
[113] Zilman, A.G., & Granek, R. Undulations and dynamic structure factor of membranes. *Phys. Rev. Lett.*, 77:4788–4791, 1996.
[114] Granek, R. From semi-flexible polymers to membranes: Anomalous diffusion and reptation. *J. Phys. II France*, 7:1761–1788, 1997.

[115] Messager, R., Bassereau, P., & Porte, G. Dynamics of the undulation mode in swollen lamellar phases. *J. Phys. France*, 51:1329–1340, 1990.
[116] Brochard, F., & Lennon, J.F. Frequency spectrum of the flicker phenomenon in erythrocytes. *J. Phys. France*, 36:1035–1047, 1975.
[117] Watson, M.C., Peng, Y., Zheng, Y., & Brown, F.L.H. The intermediate scattering function for lipid bilayer membranes: From nanometers to microns. *J. Chem. Phys.*, 135:194701, 2011.
[118] Van Kampen, N.G. *Stochastic Processes in Physics and Chemistry*. Elsevier, Amsterdam, 1992.
[119] Watson, M.C., & Brown, F.L.H. Interpreting membrane scattering experiments at the mesoscale: The contribution of dissipation within the bilayer. *Biophys. J.*, 98:L09–L11, 2010.
[120] Rheinstädter, M.C., Häußler, W., & Salditt, T. Dispersion relation of lipid membrane shape fluctuations by neutron spin-echo spectrometry. *Phys. Rev. Lett.*, 97:048103, 2006.
[121] Bivas, I., Méléard, P., Mircheva, I., & Bothorel, P. Thermal shape fluctuations of a quasi spherical lipid vesicle when the mutual displacements of its monolayers are taken into account. *Coll. Surf. A.*, 157:21–33, 1999.
[122] Miao, L., Lomholt, M.A., & Kleis, J. Dynamics of shape fluctuations of quasi-spherical vesicles revisited. *Eur. Phys. J. E.*, 9:143–160, 2002.
[123] Shkulipa, S.A., Den Otter, W.K., & Briels, W.J. Thermal undulations of lipid bilayers relax by intermonolayer friction at submicrometer length scales. *Phys. Rev. Lett.*, 96:178302, 2006.
[124] Arriaga, L.R., Rodríguez-García, R., López-Montero, I., Farago, B., Hellweg, T., & Monroy, F. Dissipative curvature fluctuations in bilayer vesicles: Coexistence of pure- bending and hybrid curvature-compression modes. *Eur. Phys. J. E.*, 31:105–113, 2010.
[125] Mell, M., Moleiro, L.H., Hertle, Y., López-Montero, I., Cao, F.J., Fouquet, P., Hellweg, T., & Monroy, F. Fluctuation dynamics of bilayer vesicles with intermonolayer sliding: Experiment and theory. *Chem. Phys. Lipids*, 185:61–77, 2015.
[126] Iñiguez-Palomares, R., Acuña-Campa, H., & Maldonado, A. Effect of polymer on the elasticity of surfactant membranes: A light scattering study. *Phys. Rev. E.*, 84:011604, 2011.
[127] Takeda, T., Kawabata, Y., Seto, H., Komura, S., Ghosh, S.K., Nagao, M., & Okuhara, D. Neutron spin-echo investigations of membrane undulations in complex fluids involving amphiphiles. *J. Phys. Chem. Solids*, 60:1375–1377, 1999.
[128] Komura, S., Takeda, T., Kawabata, Y., Ghosh, S.K., Seto, H., & Nagao, M. Dynamical fluctuation of the mesoscopic structure in ternary $C_{12}E_5$-water-n-octane amphiphilic system. *Phys. Rev. E.*, 63:041402, 2001.
[129] Seto, H., Yamada, N.L., Nagao, M., Hishida, M., & Takeda, T. Bending modulus of lipid bilayers in a liquid-crystalline phase including an anomalous swelling regime estimated by neutron spin echo experiments. *Eur. Phys. J. E.*, 26:217–223, 2008.
[130] Yi, Z., Nagao, M., & Bossev, D.P. Bending elasticity of saturated and monounsaturated phospholipid membranes studied by the neutron spin echo technique. *J. Phys.: Condens. Matter*, 21:155104, 2009.
[131] Mihailescu, M., Monkenbusch, M., Endo, H., Allgaier, J., Gompper, G., Stellbrink, J., Richter, D., Jakobs, B., Sottmann, T., & Farago, B. Dynamics of bicontinuous microemulsion phases with and without amphiphilic block-copolymers. *J. Chem. Phys.*, 115:9563–9577, 2001.
[132] Mihailescu, M., Monkenbusch, M., Allgaier, J., Frielinghaus, H., Richter, D., Jakobs, B., & Sottmann, T. Neutron scattering study on the structure and dynamics of oriented lamellar phase microemulsions. *Phys. Rev. E.*, 66:041504, 2002.
[133] Monkenbusch, M., Holderer, O., Frielinghaus, H., Byelov, D., Allgaier, J., & Richter, D. Bending moduli of microemulsions; comparison of results from small angle neutron scattering and neutron spin-echo spectroscopy. *J. Phys.: Condens. Matter*, 17:S2903–S2909, 2005.

[134] Holderer, O., Frielinghaus, H., Byelov, D., Monkenbusch, M., Allgaier, J., & Richter, D. Dynamic properties of microemulsions modified with homopolymers and diblock copolymers: The determination of bending moduli and renormalization effects. *J. Chem. Phys.*, 122:094908, 2005.
[135] Lee, J.-H., Choi, S.-M., Doe, C., Faraone, A., Pincus, P.A., & Kline, S.R. Thermal fluctuation and elasticity of lipid vesicles interacting with pore-forming peptides. *Phys. Rev. Lett.*, 105:038101, 2010.
[136] Evans, E., Yeung, A., Waugh, R., & Song, J. Dynamic coupling and nonlocal curvature elasticity in bilayer membranes. In R. Lipowsky, D. Richter, & K. Kremer, editors, *The Structure and Conformation of Amphiphilic Membranes*, pages 148–153, Berlin, 1992. Springer.
[137] Marrink, S.J., & Mark, A.E. Effect of undulations on surface tension in simulated bilayers. *J. Phys. Chem. B.*, 105:6122–6127, 2001.
[138] Brannigan, G., & Brown, F.L.H. A consistent model for thermal fluctuations and protein-induced deformations in lipid bilayers. *Biophys. J.*, 90:1501–1520, 2006.
[139] West, B., Brown, F.L.H., & Schmid, F. Membrane-protein interactions in a generic coarse-grained model for lipid bilayers. *Biophys. J.*, 96:101–115, 2009.
[140] Brandt, E.G., Braun, A.R., Sachs, J.N., Nagle, J.F., & Edholm, O. Interpretation of fluctuation spectra in lipid bilayer simulations. *Biophys. J.*, 100:2104–2111, 2011.
[141] Nagao, M., Chawang, S., & Hawa, T. Interlayer distance dependence of thickness fluctuations in a swollen lamellar phase. *Soft Matter*, 7:6598–6605, 2011.
[142] Farago, B., Monkenbusch, M., Goecking, K.D., Richter, D., & Huang, J.S. Dynamics of microemulsions as seen by neutron spin echo. *Physica B.*, 213 & 214:712–717, 1995.
[143] Farago, B. Spin echo studies of microemulsions. *Physica B.*, 226:51–55, 1996.
[144] Nagao, M. Observation of local thickness fluctuations in surfactant membranes using neutron spin echo. *Phys. Rev. E.*, 80:031606, 2009.
[145] Nagao, M. Temperature and scattering contrast dependencies of thickness fluctuations in surfactant membranes. *J. Chem. Phys.*, 135:074704, 2011.
[146] Carrillo, J.-M.Y., Katsaras, J., Sumpter, B.G., & Ashkar, R. A computational approach for modeling neutron scattering data from lipid bilayers. *J. Chem. Theory Comput.*, 13:916–925, 2017.
[147] Lemmich, J., Mortensen, K., Ipsen, J.H., Hønger, T., Bauer, R., & Mouritsen, O.G. Small-angle neutron scattering from multilamellar lipid bilayers: Theory, model, and experiment. *Phys. Rev. E.*, 53:5169–5180, 1996.
[148] Frielinghaus, H. Small-angle scattering model for multilamellar vesicles. *Phys. Rev. E.*, 76:051603, 2007.
[149] Caillé, A. Remarques sur la diffusion des rayons X dans les smectiques A. *C. R. Acad. Sci. Paris, Ser. B.*, 274:891–893, 1972.
[150] Nallet, F., Laversanne, R., & Roux, D. Modelling X-ray or neutron scattering spectra of lyotropic lamellar phases: Interplay between form and structure factors. *J. Phys. II.*, 3:487–502, 1993.
[151] de Gennes, P.G. Liquid dynamics and inelastic scattering of neutrons. *Physica.*, 25:825–839, 1959.
[152] Pfeiffer, W., König, S., Legrand, J.F., Bayerl, T., Richter, D., & Sackmann, E. Neutron spin echo study of membrane undulations in lipid multibilayers. *Europhys. Lett.*, 23:457–462, 1993.
[153] Evans, E., & Rawicz, W. Entropy-driven tension and bending elasticity in condensed- fluid membranes. *Phys. Rev. Lett.*, 64:2094–2097, 1990.
[154] Dimova, R., Aranda, S., Bezlyepkina, N., Nikolov, V., Riske, K.A., & Lipowsky, R. A practical guide to giant vesicles. Probing the membrane nanoregime via optical microscopy. *J. Phys.: Condens. Matter.*, 18:S1151–S1176, 2006.
[155] Olson, F., Hunt, C.A., Szoka, F.C., Vail, W.J., & Papahadjopoulos, D. Preparation of liposomes of defined size distribution by extrusion through polycarbonate membranes. *Biochim. Biophys. Acta*, 557:9–23, 1979.

[156] Yamada, N.L., Seto, H., Takeda, T., Nagao, M., Kawabata, Y., & Inoue, K. SAXS, SANS and NSE studies on "unbound state" in DPPC/water/$CaCl_2$ system. *J. Phys. Soc. Jpn.*, 74:2853–2859, 2005.
[157] Brüning, B., Stehle, R., Falus, P., & Farago, B. Influence of charge density on bilayer bending rigidity in lipid vesicles: A combined dynamic light scattering and neutron spin-echo study. *Eur. Phys. J. E.*, 36:77, 2013.
[158] Pan, J., Cheng, X., Sharp, M., Ho, C.-S., Khadka, N., & Katsaras, J. Structural and mechanical properties of cardiolipin lipid bilayer determined using neutron spin echo, small angle neutron and X-ray scattering, and molecular dynamics simulations. *Soft Matter*, 11:130–138, 2015.
[159] Arriaga, L.R., López-Montero, I., Monroy, F., Orts-Gil, G., Farago, B., & Hellweg, T. Stiffening effect of cholesterol on disordered lipid phases: A combined neutron spin echo + dynamic light scattering analysis of the bending elasticity of large unilamellar vesicles. *Biophys. J.*, 96:3629–3637, 2009.
[160] Brüning, B.A., Prévost, S., Stehle, R., Steitz, R., Falus, P., Farago, B., & Hellweg, T. Bilayer undulation dynamics in unilamellar phospholipid vesicles: Effect of temperature, cholesterol and trehalose. *Biochim. Biophys. Acta*, 1838:2412–2419, 2014.
[161] Hirai, M., Kimura, R., Takeuchi, K., Sugiyama, M., Kasahara, K., Ohta, N., Farago, B., Stadler, A., & Zaccai, G. Change of dynamics of raft-model membrane induced by amyloid-β protein binding. *Eur. Phys. J. E.*, 36:74, 2013.
[162] Brüning, B., & Farago, B. Perfluorooctanoic acid rigidifies a model lipid membrane. *Phys. Rev. E.*, 89:040702(R), 2014.
[163] Boggara, M.B., Faraone, A., & Krishnamoorti, R. Effect of pH and ibuprofen on phospholipid bilayer bending modulus. *J. Phys. Chem. B.*, 114:8061–8066, 2010.
[164] Yi, Z., Nagao, M., & Bossev, D.P. Effect of charged lidocaine on static and dynamic properties of model bio-membranes. *Biophys. Chem.*, 160:20–27, 2012.
[165] Hoffmann, I., Michel, R., Sharp, M., Holderer, O., Appavou, M.S., Polzer, F., Farago, B., & Gradzielski, M. Softening of phospholipid membranes by the adhesion of silica nanoparticles – as seen by neutron spin-echo (NSE). *Nanoscale*, 6:6945–6952, 2014.
[166] Mell, M., Moleiro, L.H., Hertle, Y., Fouquet, P., Schweins, R., López-Montero, I., Hellweg, T., & Monroy, F. Bending stiffness of biological membranes: What can be measured by neutron spin echo? *Eur. Phys. J. E.*, 36:75, 2013.
[167] Moleiro, L.H., Mell, M., Bocanegra, R., López-Montero, I., Fouquet, P., Hellweg, T., Carrascosa, J.L., & Monroy, F. Permeability modes in fluctuating lipid membranes with DNA-translocating pores. *Adv. Coll. Int. Sci.*, 247:543–554, 2017.
[168] Nickels, J.D., Cheng, X., Mostofian, B., Stanley, C., Lindner, B., Heberle, F.A., Perticaroli, S., Feygenson, M., Egami, T., Standaert, R.F., Smith, J.C., Myles, D.A.A., Ohl, M., & Katsaras, J. Mechanical properties of nanoscopic lipid domains. *J. Am. Chem. Soc.*, 137:15772–15780, 2015.
[169] Stingaciu, L.R., O'Neill, H., Liberton, M., Urban, V.S., Pakrasi, H.B., & Ohl, M. Revealing the dynamics of thylakoid membranes in living cyanobacterial cells. *Sci. Rep.*, 6:19627, 2016.
[170] Nickels, J.D., Chatterjee, S., Mostofian, B., Stanley, C.B., Ohl, M., Zolnierczuk, P., Schulz, R., Myles, D.A.A., Standaert, R.F., Elkins, J.G., Cheng, X., & Katsaras, J. *Bacillus subtilis* lipid extract, a branched-chain fatty acid model membrane. *J. Phys. Chem. Lett.*, 8:4214–4217, 2017.
[171] Boal, D. *Mechanics of the Cell*. Cambridge University Press, 2nd edition, Cambridge, UK, 2002.
[172] Baumgart, T., Das, S., Webb, W.W., & Jenkins, J.T. Membrane elasticity in giant vesicles with fluid phase coexistence. *Biophys. J.*, 89:1067–1080, 2005.
[173] Bitbol, A.-F., Constantin, D., & Fournier, J.-B. Bilayer elasticity at the nanoscale: The need for new terms. *PLOS One.*, 7:e48306, 2012.
[174] Hu, M., de Jong, D.H., Marrink, S.J., & Deserno, M. Gaussian curvature elasticity determined from global shape transformations and local stress distributions: A comparative study using the MARTINI model. *Faraday Discuss.*, 161:365–382, 2013.

[175] Venable, R.M., Brown, F.L.H., & Pastor, R.W. Mechanical properties of lipid bilayers from molecular dynamics simulation. *Chem. Phys. Lipids*, 192:60–74, 2015.
[176] Rand, R.P., & Fuller, N.L. Structural dimensions and their changes in a reentrant hexagonal-lamellar transition of phospholipids. *Biophys. J.*, 66:2127–2138, 1994.
[177] Leikin, S., Kozlov, M.M., Fuller, N.L., & Rand, R.P. Measured effects of diacylglycerol on structural and elastic properties of phospholipid membranes. *Biophys. J.*, 71:2623–2632, 1996.
[178] Winterhalter, M., & Helfrich, W. Bending elasticity of electrically charged bilayers: Coupled monolayers, neutral surfaces, and balancing stresses. *J. Phys. Chem.*, 96:327–330, 1992.
[179] Templer, R.H., Khoo, B.J., & Seddon, J.M. Gaussian curvature modulus of an amphiphilic monolayer. *Langmuir*, 14:7427–7434, 1998.
[180] Campelo, F., McMahon, H.T., & Kozlov, M.M. The hydrophobic insertion mechanism of membrane curvature generation by proteins. *Biophys. J.*, 95:2325–2339, 2008.
[181] Campelo, F., Arnarez, C., Marrink, S.J., & Kozlov, M.M. Helfrich model of membrane bending: From Gibbs theory of liquid interfaces to membranes as thick anisotropic elastic layers. *Adv. Colloid Interface Sci.*, 208:25–33, 2014.
[182] Kollmitzer, B., Heftberger, P., Rappolt, M., & Pabst, G. Monolayer spontaneous curvature of raft-forming membrane lipids. *Soft Matter*, 9:10877–10884, 2013.
[183] Wu, Y., Štefl, M., Olzyńska, A., Hof, M., Yahioglu, G., Yip, P., Casey, D.R., Ces, O., Humpolíčková, J., & Kuimova, M.K. Molecular rheometry: Direct determination of viscosity in L_O and L_D lipid phases via fluorescence lifetime imaging. *Phys. Chem. Chem. Phys.*, 15:14986–14993, 2013.
[184] Nagao, M., Kelley, E.G., Ashkar, R., Bradbury, R., & Butler, P.D. Probing elastic and viscous properties of phospholipid bilayers using neutron spin echo spectroscopy. *J. Phys. Chem. Lett.*, 8:4679–4684, 2017.
[185] Doktorova, M., Harries, D., & Khelashvili, G. Determination of bending rigidity and tilt modulus of lipid membranes from real-space fluctuation analysis of molecular dynamics simulations. *Phys. Chem. Chem. Phys.*, 19:16806–16818, 2017.
[186] Méléard, P., Gerbeaud, C., Pott, T., Fernandez-Puente, L., Bivas, I., Mitov, M.D., Dufourcq, J., & Bothorel, P. Bending elasticities of model membranes: Influences of temperature and sterol content. *Biophys. J.*, 72:2616–2629, 1997.
[187] Nagle, J.F., Jablin, M.S., Tristram-Nagle, S., & Akabori, K. What are the true values of the bending modulus of simple lipid bilayers? *Chem. Phys. Lipids*, 185:3–10, 2015.
[188] Rawicz, W., Olbrich, K.C., McIntosh, T., Needham, D., & Evans, E. Effect of chain length and unsaturation on elasticity of lipid bilayers. *Biophys. J.*, 79:328–339, 2000.
[189] Pan, J., Tristram-Nagle, S., & Nagle, J.F. Effect of cholesterol on structural and mechanical properties of membranes depends on lipid chain saturation. *Phys. Rev. E.*, 80:021931, 2009.
[190] Bradbury, R., & Nagao, M. Effect of charge on the mechanical properties of surfactant bilayers. *Soft Matter*, 12:9383–9390, 2016.
[191] Lee, V., & Hawa, T. Investigation of the effect of bilayer membrane structures and fluctuation amplitudes on SANS/SAXS profile for short membrane wavelength. *J. Chem. Phys.*, 139:124905, 2013.
[192] Allen, M.P., & Tildesley, D.J. *Computer Simulation of Liquids*. Oxford Science Publications, Oxford, 1987.
[193] Braganza, L.F., & Worcester, D.L. Structural changes in lipid bilayers and biological membranes caused by hydrostatic pressure. *Biochemistry*, 25:7484–7488, 1986.
[194] Nagle, J.F., & Wilkinson, D.A. Lecithin bilayers. Density measurements and molecular interactions. *Biophys. J.*, 23:159–175, 1978.
[195] Koenig, B.W., & Gawrisch, K. Specific volumes of unsaturated phosphatidylcholines in the liquid crystalline lamellar phase. *Biochim. Biophys. Acta*, 1715:65–70, 2005.

[196] Nagle, J.F., & Tristram-Nagle, S. Structure of lipid bilayers. *Biochim. Biophys. Acta*, 1469:159–195, 2000.
[197] Kučerka, N., Nieh, M.P., & Katsaras, J. Fluid phase lipid areas and bilayer thicknesses of commonly used phosphatidylcholines as a function of temperature. *Biochim. Biophys. Acta*, 1808:2761–2771, 2011.
[198] Kučerka, N., Heberle, F.A., Pan, J., & Katsaras, J. Structural significance of lipid diversity as studied by small angle neutron and X-ray scattering. *Membranes*, 5:454–472, 2015.
[199] Barker, J.G., & Pedersen, J.S. Instrumental smearing effects in radially symmetric small-angle neutron scattering by numerical and analytical methods. *J. Appl. Crystallogr.*, 28:105–114, 1995.
[200] Dymond, J.H., & Øye, H.A. Viscosity of selected liquid n-alkanes. *J. Phys. Chem. Ref. Data*, 23:41–53, 1994.
[201] Doolittle, A.K. Studies of Newtonian flow. I. The dependence of the viscosity of liquids on temperature. *J. Appl. Phys.*, 22:1031–1035, 1951.
[202] Dimova, R., Dietrich C., Hadjisky A., Danov K., and Pouligny B. Falling ball viscosimetry of giant vesicle membranes: Finite-size effects. *Eur. Phys. J. B.*, 12:589–598, 1999.
[203] Petrov, E.P., Petrosyan, R., & Schwille, P. Translational and rotational diffusion of micrometer-sized solid domains in lipid membranes. *Soft Matter*, 8:7552–7555, 2012.
[204] Camley, B.A., Esposito, C., Baumgart, T., & Brown, F.L.H. Lipid bilayer domain fluctuations as a probe of membrane viscosity. *Biophys. J.*, 99:L44–L46, 2010.
[205] Honerkamp-Smith, A.R., Woodhouse, F.G., Kantsler, V., & Goldstein, R.E. Membrane viscosity determined from shear-driven flow in giant vesicles. *Phys. Rev. Lett.*, 111:038103, 2013.
[206] Stanich, C.A., Honerkamp-Smith, A.R., Putzel, G.G., Warth, C.S., Lamprecht, A.K., Mandal, P., Mann, E., Hua, T.-A.D., & Keller, S.L. Coarsening dynamics of domains in lipid membranes. *Biophys. J.*, 105:444–454, 2013.
[207] Hormel, T.T., Kurihara, S.Q., Brennan, M.K., Wozniak, M.C., & Parthasarathy, R. Measuring lipid membrane viscosity using rotational and translational probe diffusion. *Phys. Rev. Lett.*, 112:188101, 2014.
[208] Waugh, R., & Evans, E.A. Thermoelasticity of red blood cell membrane. *Biophys. J.*, 26:115–131, 1979.
[209] Hochmuth, R.M., Buxbaum, K.L., & Evans, E.A. Temperature dependence of the viscoelastic recovery of red cell membrane. *Biophys. J.*, 29:177–182, 1980.
[210] Rahimi, M., & Arroyo, M. Shape dynamics, lipid hydrodynamics, and the complex viscoelasticity of bilayer membranes. *Phys. Rev. E.*, 86:011932, 2012.
[211] Tristram-Nagle, S., Liu, Y., Legleiter, J., & Nagle, J.F. Structure of gel phase DMPC determined by X-ray diffraction. *Biophys. J.*, 83:3324–3335, 2002.
[212] Chiantia, S., & London, E. Acyl chain length and saturation modulate interleaflet coupling in asymmetric bilayers: Effects on dynamics and structural order. *Biophys. J.*, 103:2311–2319, 2012.
[213] Liu, Y., & Nagle, J.F. Diffuse scattering provides material parameters and electron density profiles of biomembranes. *Phys. Rev. E.*, 69:040901(R), 2004.
[214] Nagle, J.F. X-ray scattering reveals molecular tilt is an order parameter for the main phase transition in a model biomembrane. *Phys. Rev. E.*, 96:030401(R), 2017.